



UPPSALA
UNIVERSITET

*Digital Comprehensive Summaries of Uppsala Dissertations
from the Faculty of Medicine 1139*

Characterization of [¹⁸F]flutemetamol binding properties

A β -amyloid PET imaging ligand

KERSTIN HEURLING



ACTA
UNIVERSITATIS
UPSALIENSIS
UPPSALA
2015

ISSN 1651-6206
ISBN 978-91-554-9356-1
urn:nbn:se:uu:diva-262019

Dissertation presented at Uppsala University to be publicly examined in Skoogsalen, Akademiska Sjukhuset, Ingång 79, Uppsala, Thursday, 19 November 2015 at 09:15 for the degree of Doctor of Philosophy (Faculty of Medicine). The examination will be conducted in English. Faculty examiner: Professor Julie Price (University of Pittsburgh).

Abstract

Heurling, K. 2015. Characterization of [^{18}F]flutemetamol binding properties. A β -amyloid PET imaging ligand. *Digital Comprehensive Summaries of Uppsala Dissertations from the Faculty of Medicine* 1139. 74 pp. Uppsala: Acta Universitatis Upsaliensis. ISBN 978-91-554-9356-1.

The criteria for diagnosing Alzheimer's disease (AD) have recently been revised to include the use of biomarkers for the *in vivo* presence of β -amyloid, one of the neuropathological hallmarks of AD. Examples of such biomarkers are positron emission tomography (PET) β -amyloid specific ligands, including [^{18}F]flutemetamol. The aim of this thesis was to characterize the binding properties of [^{18}F]flutemetamol from a tracer kinetic perspective as well as by validating binding measures through comparison with tissue pathology assessments. The applicability of previously developed kinetic models of tracer binding for voxel-based analysis was examined and compared to arterial input compartment modelling, the "gold standard" for PET quantification. Several voxel-based methods were found to exhibit high correlations with compartment modelling, including the semi-quantitative standardized uptake value ratio (SUVR). The kinetic components of [^{18}F]flutemetamol uptake were also investigated without model assumptions using the data driven method spectral analysis, with binding to β -amyloid shown to relate to a slow kinetic component. The same component was also found to predominate in the uptake of white matter, known to be free of β -amyloid accumulation. White matter uptake was however possible to separate from β -amyloid binding based on the relative contribution of the slow component to the total volume of distribution. Uptake of [^{18}F]flutemetamol as quantified using SUVR or assessed visually was found to correlate well with tissue pathology assessments. Classifying the brains of 68 deceased subjects who had undergone [^{18}F]flutemetamol PET scanning *ante mortem*, based on the spatial distribution of β -amyloid according to pre-defined phases, revealed that abnormal uptake patterns of [^{18}F]flutemetamol were only certain to be found in the last phase of β -amyloid accumulation. In the same cohort however, [^{18}F]flutemetamol was also shown to accurately distinguish between subjects with AD and non-AD dementia. While this supports the use of [^{18}F]flutemetamol in clinical settings for ruling out AD, the association of abnormal [^{18}F]flutemetamol uptake to late phases of β -amyloid accumulation may limit the detection of early accumulation and pre-clinical stages of AD. It remains to be investigated whether application of voxel-based methods and slow component filtering may increase sensitivity, particularly in the context of clinical trials.

Keywords: Positron emission tomography (PET), molecular imaging, amyloid, tracer validation

Kerstin Heurling, Department of Surgical Sciences, Radiology, Akademiska sjukhuset, Uppsala University, SE-75185 Uppsala, Sweden.

© Kerstin Heurling 2015

ISSN 1651-6206

ISBN 978-91-554-9356-1

urn:nbn:se:uu:diva-262019 (<http://urn.kb.se/resolve?urn=urn:nbn:se:uu:diva-262019>)

*If we knew what it was we were doing, it
wouldn't be called research, would it?*

Albert Einstein

List of Papers

This thesis is based on the following papers, which are referred to in the text by their Roman numerals.

- I Heurling, K., Buckley, C., Van Laere, K., Vandenberghe, R. and Lubberink, M. (2015) Parametric imaging and quantitative analysis of the PET amyloid ligand [^{18}F]flutemetamol. *Neuroimage*, 121:184-192
- II Heurling, K., Buckley, C., Vandenberghe, R., Van Laere, K. and Lubberink, M. (2015) Separation of β -amyloid binding and white matter uptake of [^{18}F]flutemetamol using spectral analysis. *AJNMMI*, In press
- III Senda, M., Yamamoto, Y., Sasaki, M., Yamane, T., Brooks, D.J., Farrar, G., McParland, B. and Heurling, K. (2015) An exploratory study of the amyloid imaging agent [^{18}F]flutemetamol in Japanese subjects. *Ann Nucl Med*, 29(5):391–399
- IV Leinonen, V., Rinne, J.O., Virtanen, K.A., Eskola, O., Rummukainen, J., Huttunen, J., von und zu Fraunberg, M., Nerg, O., Koivisto, A. M., Rinne, J., Jääskeläinen, J. E., Buckley, C., Smith, A., Jones, P. A., Sherwin, P., Farrar, G., McLain, R., Kailajärvi, M., Heurling, K. and Grachev I. D. (2013) Positron emission tomography with [^{18}F]flutemetamol and [^{11}C]PiB for in vivo detection of cerebral cortical amyloid in normal pressure hydrocephalus patients. *Eur. J. Neurol*, 20(7):1043-1052
- V Leinonen, V., Rinne, J.O., Wong, D.F., Wolk, D.A., Trojanowski, J.Q., Sherwin, P.F., Smith, A., Heurling, K., Su, M. and Grachev. I.D. (2014) Diagnostic effectiveness of quantitative [^{18}F]flutemetamol PET imaging for detection of fibrillary amyloid β using cortical biopsy histopathology as the standard of truth in subjects with idiopathic normal pressure hydrocephalus. *Acta Neuropath Commun*, 2(1):46
- VI Thal, D.R., Beach, T.G., Zante, M., Heurling, K., Chakrabarty, A., Ismail, A., Smith, A.P.L. and Buckley, C. (2015) [^{18}F]flutemetamol amyloid positron emission tomography in preclinical and symptomatic Alzheimer's disease: Specific detection of advanced phases of amyloid- β pathology. *Alzheimer's Dement*, 11(8):975-985

Reprints were made with permission from the respective publishers.

Contents

| | |
|--|----|
| Introduction | 11 |
| Positron emission tomography | 11 |
| Fundamentals | 11 |
| Quantification of PET | 13 |
| Alzheimer's disease | 18 |
| Clinical diagnosis of AD | 19 |
| Pathophysiology of AD | 21 |
| AD and idiopathic normal pressure hydrocephalus | 21 |
| β -amyloid PET imaging | 22 |
| $[^{18}\text{F}]$ Flutemetamol | 23 |
| Use of β -amyloid PET imaging ligands beyond AD | 27 |
| Summary | 28 |
| Aims of the thesis | 29 |
| Materials and methods | 31 |
| Research participants | 31 |
| Study design | 32 |
| Scanning procedures | 32 |
| Radiochemistry | 33 |
| Tissue analysis | 34 |
| Biopsy procedures | 34 |
| Autopsy procedures | 34 |
| Efficacy analysis | 35 |
| Clinicopathologic classification of end-of-life patients | 36 |
| Image data analysis | 36 |
| Image processing | 36 |
| Blinded visual image assessments | 37 |
| VOI definitions | 37 |
| Partial volume effects correction | 39 |
| Kinetic modelling | 39 |
| Spectral analysis | 40 |
| Parametric images | 40 |
| Simulation studies | 41 |
| Statistical analyses | 42 |

| | |
|---|----|
| Results | 44 |
| Kinetic properties of [^{18}F]flutemetamol | 44 |
| Basic quantification of [^{18}F]flutemetamol uptake..... | 44 |
| Spectral analysis for characterization of tracer binding..... | 45 |
| Parametric images of [^{18}F]flutemetamol uptake | 46 |
| Simulation studies | 48 |
| Validation of [^{18}F]flutemetamol with neuropathology | 50 |
| <i>In vivo</i> cortical biopsies | 50 |
| <i>Post mortem</i> tissue sampling | 52 |
| Discussion | 54 |
| Future perspectives | 58 |
| Concluding remarks | 60 |
| Summary in Swedish..... | 61 |
| Acknowledgements | 63 |
| Bibliography..... | 65 |

Abbreviations

| | |
|------------------|--|
| 1-TC | 1-tissue compartment model |
| 2-TC | 2-tissue compartment model |
| 3-TC | 3-tissue compartment model |
| AD | Alzheimer's disease |
| aMCI | amnesic mild cognitive impairment |
| BP _{ND} | binding potential |
| BSS | modified Bielschowsky silver stain |
| CAA | cerebral amyloid angiopathy |
| CERAD | Consortium to Establish a Registry for Alzheimer's disease |
| CoV | coefficient of variation |
| CSF | cerebrospinal fluid |
| CT | computed tomography |
| DLB | dementia with Lewy bodies |
| DVR | distribution volume ratio |
| FN | false negative |
| FP | false positive |
| FTD | frontotemporal dementia |
| FTLD-tau | frontotemporal lobar degeneration with tau inclusions |
| HC | histochemistry |
| HV | healthy volunteers |
| ICP | intracranial pressure |
| IHC | immunohistochemistry |
| iNPH | idiopathic normal pressure hydrocephalus |
| MCI | mild cognitive impairment |
| MRI | magnetic resonance imaging |
| MRTM | multilinear reference tissue model |
| MS | multiple sclerosis |
| NFT | neurofibrillary tangle |
| NIA-AA | National Institute of Aging and Alzheimer's Association |

| | |
|----------------------|---|
| NINCDS-ADRDA | National Institute of Neurological and Communicative Disorders and Stroke and the Alzheimer's Disease and Related Disorders Association |
| NPV | negative predictive value |
| pAD | probable Alzheimer's disease (clinical diagnosis) |
| PET | positron emission tomography |
| p.i. | post injection |
| PPV | positive predictive value |
| PVE | partial volume effects |
| ROC | receiver operating characteristic |
| RPM | receptor parametric mapping |
| RPM2 | receptor parametric mapping, 2 parameters |
| SA | spectral analysis |
| SOT | standard of truth |
| SRTM | simplified reference tissue model |
| SRTM2 | simplified reference tissue model, 2 parameters |
| SUV | standardized uptake value |
| SUVR | standardized uptake value ratio |
| SUVR _{CER} | standardized uptake value ratio using cerebellar cortex as reference region |
| SUVR _{PONS} | standardized uptake value ratio using pons as reference region |
| TAC | time activity curve |
| TN | true negative |
| TP | true positive |
| VOI | volume of interest |
| V _T | total volume of distribution |

Introduction

Alzheimer's disease (AD) is the most common cause of dementia, accounting for approximately two-thirds of all cases. This incurable, degenerative, and terminal disease was first described by the German psychiatrist and neuropathologist Alois Alzheimer in 1906 and was named after him. Although we know that AD and other neurodegenerative entities are distinct diseases, in their early stages they can prove difficult to differentiate.

Traditionally, diagnostic imaging was restricted to the visualization of brain structures using computed tomography (CT) and magnetic resonance imaging (MRI). However, since proteinopathies can develop in the absence of macroscopic changes, methods better suited for imaging alterations in brain function had to be developed. Molecular imaging tracers for use with positron emission tomography (PET) provide the basis not only for a better understanding of molecular processes in the brain, but also for classification of patients for the development of individualized therapies. PET tracers targeting neuropathological hallmarks of AD have been developed to aid in the diagnosis of AD, such as those binding to aggregated forms of β -amyloid.

β -amyloid deposition is believed to begin in cognitively normal elderly subjects who may subsequently develop signs of mild cognitive impairment (MCI) and could then finally develop AD dementia, in whom *post mortem* analysis demonstrates the characteristic abundance of β -amyloid plaques in specific brain areas. The time course of β -amyloid deposition, and the temporal offset in terms of subsequent cognitive decline suggests that β -amyloid imaging could help determine the appropriate time for intervention with drugs targeting β -amyloid.

This thesis aims to summarize and discuss part of the process of characterizing and validating a new PET tracer for use in the clinical evaluation of AD.

Positron emission tomography

Fundamentals

PET is a functional imaging technique, providing insight into physiological, biochemical and pharmacological processes *in vivo*. Through administration of molecules in tracer amounts labelled with short-lived radioactive positron-

emitting isotopes such as carbon-11, fluorine-18 and oxygen-15, the spatial and temporal distribution of these molecules in tissues of interest can be measured in the PET scanner without affecting the biological system. The administration of the radiolabelled tracer can be performed via several administration routes, including inhalation or oral administration. This thesis, however, will only include the case of intravenous tracer injection into the blood stream.

The PET scanner detects coincidences, i.e. simultaneous pairs of 511 keV photons, emitted in opposite directions when the positron released by the isotope within a labelled molecule is annihilated in the collision with an atomic electron a short distance from the decay of the nucleus, as illustrated in Figure 1 A. By means of computerized mathematical reconstruction methods, the detected counts can, after correction for a number of factors such as photon attenuation, scatter and random coincidences, be transformed into an image showing the spatial distribution of the radioactive decay, i.e. the distribution of tracer in the unit of radioactivity concentration in a tissue (Bq/mL) [1]. By collecting the data in a series of consecutive time windows, so called frames, the change of the distribution over time can be followed in a dynamic PET scan. Assessment of PET images often focuses on a specific region or a volume of interest (VOI), covering a number of voxels in the image and giving one estimate of the tracer uptake in the VOI given by the average radioactivity concentration of the included voxels. VOIs are defined on the PET data in dedicated software either manually, through thresholding or by means of pre-defined probabilistic anatomical atlases that enable

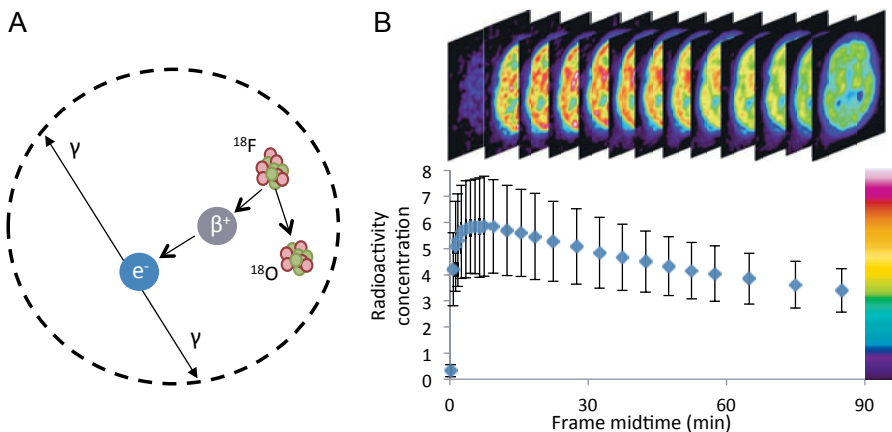


Figure 1. A) Schematic drawing of the two-step emission of γ -rays from the disintegration of the unstable fluorine-18 atom to stable oxygen-18 within a ring of detectors. The distance between the fluorine atom and the annihilation is greatly exaggerated. B) The collection of data in frames during a dynamic PET scan from the start of injection and for 90 min. The graph shows the time-activity curve for the whole brain uptake, with higher standard deviations early in the scan due to shorter frames.

identical VOIs to be applied to multiple subjects. The latter approach is often used when studying the brain. The measured radioactivity in a voxel or VOI throughout the time course of the dynamic PET scan provides a time activity curve (TAC), showing the uptake, temporal distribution, retention and clearance of the tracer over time, as illustrated in Figure 1 B.

PET has a wide variety of applications. In clinical routine practice it is often used especially in the field of oncology and a number of different tracers have been developed targeting physiological processes in tumours. The most widely used tracer in oncology diagnostics is [^{18}F]fluorodeoxyglucose [2]. The diagnostic use of PET is also increasing in neurological disorders such as Parkinsonian syndromes [3-5] and AD, which will be further discussed in this thesis. In addition, PET has become an important tool in drug development, studying distribution of drug candidates, pharmacodynamic effects in the form of receptor occupancy and as a biomarker for physiological response to drug candidates. Last but not least, PET is used extensively in basic research in order to provide an increased understanding of physiological processes such as endogenous neurotransmission [6,7].

Quantification of PET

Compartment modelling

After injection, the tracer distributes throughout the body within the blood pool and tissues. The signal measured by the PET scanner is the sum of several states of the PET tracer: tracer in the blood pool that has yet to enter the tissue, metabolites of the tracer that still carry the radioactive label, and tracer within the tissue bound to the intended target but also unbound or bound non-specifically within tissue, see Figure 2 A. The target, to which the tracer binds specifically, is often an endogenous protein such as a neuroreceptor or aggregates of proteins like β -amyloid indicative of a pathological process. In order to separate these signals to estimate the parameter of interest, i.e. binding to the intended target, kinetic modelling is applied, characterizing the rate at which the tracer distributes.

The transition, accumulation and washout in the different states, called compartments, of the tracer can be described by first order differential equations [8,9]. The tissues of interest are exposed to the tracer from the plasma compartment supply, throughout the time course of the PET scan or as long as the tracer remains unmetabolized in the blood stream, with the rate of the delivery denoted K_1 . The aim is therefore to determine the time course of the compartments, based on the known input concentration in plasma, which varies over time and which can be measured by blood sampling.

Depending on the characteristics of the tracer - whether it binds specifically to a molecule within the tissue, and if so if the binding is reversible or irreversible during the time course of the PET scan - a mathematical model

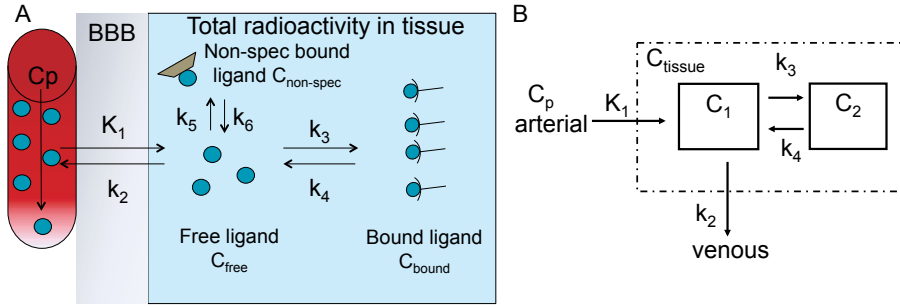


Figure 2. A) Tracer in the blood stream with the concentration C_p enters the brain through the blood brain barrier (BBB), described by the influx rate constant, K_1 and then leaves the brain, described by the efflux rate constant, k_2 . Tracer within the brain equilibrates between being free (C_{free}) and specifically bound to the target (C_{bound}) or non-specifically bound ($C_{non-spec}$) with the association and dissociation rate constants k_3 and k_4 , k_5 and k_6 , respectively. B) The 2-tissue compartment model shown as a schematic box drawing used to illustrate the different states of the tracer, where C_1 represents combined C_{free} and $C_{non-spec}$, and C_2 represents C_{bound} .

is chosen describing the compartment concentrations with the appropriate set of differential equations. Typically, although it is a simplification of the actual physiological process, three tissue compartments and one plasma compartment describe the fate of the tracer well. The model is called the 3-tissue compartment model (3-TC), with the three compartments representing the fraction of tracer free in tissue, bound specifically to the target and bound non-specifically. With the input concentration, the response in the tissue and the assumed model, the rate constants of transition between the different compartments can be estimated by fitting of the operational equation of the model to the experimental data. By collapsing the two compartments representing non-specific binding and free tracer, which is often so quickly transitioning that they cannot be accurately quantified separately, and replacing them with one compartment representing the non-displaceable tracer, the 3-TC is replaced by a 2-tissue compartment model (2-TC) [9], as shown in Figure 2B.

Relating the rate constants of the compartment modelling to pharmacological parameters such as receptor concentration (B_{max}) and association and dissociation rates (k_{on} and k_{off} , respectively), physiological parameters can be estimated. The ratio of k_3/k_4 is often referred to as the non-displaceable binding potential (BP_{ND}), which describes the targets available for tracer binding for reversibly binding tracers [8].

In some cases BP_{ND} cannot be estimated reliably, and instead the total volume of distribution (V_T) is estimated, representing a volume given by the relationship of concentrations in the plasma input and tissue studied which is equivalent to:

$$V_T = K_1/k_2 (1 + k_3/k_4) \quad (1)$$

If there is a region that is devoid of target proteins available for specific binding of the tracer, its kinetics can be described by a 1-tissue compartment model (1-TC) where V_T is instead described by:

$$V_T = K_1/k_2 \quad (2)$$

The compartment modelling approach is often regarded the “gold standard” of PET quantification, as it uses the actual plasma concentration for input function and is widely used. There are however alternative methods for estimating the binding of tracer to target as well.

Multiple-time graphical analysis

The non-linear least squares curve fitting procedures of compartment modelling is a computationally demanding procedure, and may exhibit convergence problems associated with the iterative approach. The compartment models are also dependent on the assumptions of the underlying compartment model chosen. A graphical method for reversible tracers was thus developed, known as the Logan plot or arterial input Logan [10]. This method relates the radioactivity concentration within a VOI (C_{VOI}) to the plasma concentration (C_p) by plotting $[C_{VOI} / C_{VOI}]$ against $[C_p / C_{VOI}]$ in each frame, revealing a linear relationship as equilibrium is reached. The slope of the linear regression line provides an estimate of V_T . Similar approach has also been applied to irreversibly binding tracers [11,12].

The graphical models have the benefit of being free of assumptions of tracer kinetics beyond whether the tracer binds reversibly or irreversibly, and is also less computationally demanding. Graphical models, however, tend to be sensitive to statistical noise, causing underestimation of V_T [13] where the magnitude of the underestimation depends on the magnitude of V_T itself.

Using reference regions

Due the sensitivity to noise in the direct determination of BP_{ND} , an indirect approach can be used. This works under the assumption that there is a reference tissue devoid of the tracer target, i.e. no specific binding occurs, and the kinetics should thus be best described by a 1-TC [14-17]. In addition, free tracer, non-specific binding and the influx and efflux are assumed to be the same in both target (K_1 and k_2) and reference tissue (K_1' and k_2'). By combining Eq. 1 and 2 the following is thus given:

$$V_{T, target}/V_{T, reference} = 1 + k_3/k_4 \quad (3)$$

This relationship leads to the conclusion that the ratio of total volumes of distribution (DVR) is related to BP_{ND} , such that $DVR-1$ is equal to BP_{ND} . Since quantification of the tracer binding to its intended target using com-

partment modelling requires a metabolite corrected plasma input function, arterial blood sampling is needed. Due the invasive and labour intensive nature of arterial sampling, reference tissue models were developed where the target tissue TAC is instead described as a function of the TAC in a reference tissue following the same argumentation as stated above. Different models have been developed with different underlying assumptions including simplified reference tissue models (SRTM and SRTM2) [14,18], reference input Logan [19] and multilinear reference tissue models (MRTM) [20,21].

Spectral analysis

As previously mentioned, the need for predefinition of the kinetic behaviour of a tracer in compartment modelling is a limitation of the methodology, which can cause significant errors leading to model failure. Circumventing the need for such assumptions, a data driven method called spectral analysis (SA) was created [22-24]. The method provides a spectrum of kinetic components that relate the tissue radioactivity concentration to that measured in plasma. The components come from a set of pre-defined basis functions where the exponential functions are coupled with convolution integrals. The spectrum thus consists of a number of peaks, described by α (min^{-1}) and β (min^{-1}).

$$\text{IRF}(t) = \sum_{i=1}^k \alpha_i \cdot e^{-\beta_i t} \quad (4)$$

The non-linear estimation problem of the differential equation describing the tissue radioactivity concentration as measured by the PET scanner is converted into a linear optimization problem with a fixed number of β . SA uses the arterial plasma concentration of the tracer as input and provides an estimate of V_T as well as identifying the number of kinetic components, and the associated kinetic rates, α . However, SA also works under some assumptions; it applies only to data that can be expressed with positive coefficients α . While the number of basis functions defined is usually large, spanning over a wide kinetic range, most basis functions will have a solution with $\alpha=0$.

Unlike compartment modelling, SA does not require kinetically homogeneous tissues; instead it returns all detected kinetic components within a defined region.

Semi-quantitative measurements of tracer uptake

The methods so far discussed all require dynamic scanning starting at the time of injection and a fairly long scanning duration. Semi-quantitative estimates can however be acquired over shorter time-windows, frame-by-frame or using frame summation. The summation of frames results in a static im-

age, with improved count statistics, and provides an average for the time-window over which the frames have been summed. One approach is to normalize the measured radioactivity concentration to patient body weight and administered radioactivity, resulting in a standardized uptake value (SUV) [25]. This is commonly used within oncology, and is a unitless estimate of the degree of tracer accumulation. $SUV=1$ in a VOI indicates that the concentration is what it would be with completely homogenous distribution throughout the body. $SUV>1$ indicates an accumulation of the tracer in the tissue and $SUV<1$ indicates a limited delivery in that particular tissue.

More common in neurological studies is to relate the radioactivity concentration in a target region to that of a reference region under the same assumptions as previously discussed, acquiring an SUV ratio (SUV_R) which reflects the relative contribution of specific and non-specific binding as represented by the reference region. This is an attractive alternative to kinetic modelling for estimation of tracer uptake, especially in clinical settings, as it does not require arterial cannulation or long scanning durations, and removes variability in the measured signal from sources such as administered radioactivity and body weight, similar to SUV, but also body composition [25]. This approach likewise requires a reference region unaffected by the physiologic process of interest, however SUV_R may vary with time if the uptake of the target and reference regions do not exhibit the same rate of tracer washout. It is therefore crucial that the time window for estimation of the SUV_R is validated.

Parametric imaging

The quantification mentioned thus far has focused on regional uptake in VOIs. This approach is limited in that the information within the PET data is reduced to a pre-defined set of anatomical regions, disregarding heterogeneity within those regions. Instead, kinetic models can be applied on the highest level of detail, i.e. on the voxel level, providing a static image where the numerical value of each voxel represents a physiological parameter, such as BP_{ND} , instead of radioactivity concentration, at the same spatial resolution as the original PET images. These images are called parametric images. While eliminating the bias of pre-defining the studied regions, voxel-based analysis has a disadvantage in that TACs from voxels have a much higher noise level than those within VOIs, which may affect the accuracy of the quantification.

Adaptions of previously established models for PET quantifications were made to decrease the sensitivity to noise in the voxel TACs. Basis function implementations of SRTM and SRTM2 were developed [18,26], transforming the non-linear problem to a linear equation to be solved with linear least squares for each basis function, thereby decreasing sensitivity to noise and computational requirements. While essentially the same as SRTM and SRTM2, the basis function implementations of the models are often called receptor parametric mapping (RPM and RPM2, respectively). The number of

parameters estimated in RPM2 is reduced by fixing the reference tissue efflux rate constant (k_2') based on RPM estimates in order to decrease the introduction of quantification errors due to statistical noise. Similar to RPM2, the number of estimated parameters is reduced for MRTM2 by using a fixed value for k_2' based on the average k_2' from the MRTM model.

Noise sensitivity is also an issue in the application of graphical linearization methods on voxel-level [13] that has been addressed through a reduction of the numbers of parameters estimated [20] or by application of a noise reducing filter prior to the voxel-wise model application.

Partial volume effects

As a consequence of the low spatial resolution in PET, the measured radioactivity concentration in a voxel reflects tracer uptake not only in that particular voxel but also in neighbouring voxels. This is known as partial volume effects (PVE) and is dependent on scanner characteristics as well as on the size and shape of the anatomical structures under study [27]. A schematic illustration of the impact of PVE on radioactivity measurements in a PET image is shown in Figure 3. A number of methods have been developed for correction of PVE, most utilizing more detailed anatomical information from MRI based segmentation of the brain into grey and white matter and cerebrospinal fluid (CSF) (i.e. into brain and non-brain) [28-30]. The application of PVE correction has been proposed to increase the ability to detect small changes in tracer uptake and improve quantitative accuracy, but is sensitive to the accuracy in the segmentation and image registration procedures [31,32]. Dedicated software packages, such as PVElab [33] have been developed for the correction of PVE utilizing a number of methods.

Alzheimer's disease

AD is the leading cause of dementia, accounting for 60-80% of the all dementia cases [34]. Worldwide, dementia was estimated to affect 35.6 million people in 2010, a number expected to exceed 130 million by 2050 due to population growth and increased life expectancy [35].

AD is characterized by an insidious and progressive decline in cognition including early deficits in memory, attention and language, and by the presence of neuropathological hallmarks, including extracellular deposition of β -amyloid and intracellular accumulation of tau. On clinical grounds alone, AD can be difficult to differentiate from certain focal cortical syndromes [36]. Further, in patients presenting with MCI, i.e. cognitive decline but no dementia, it can prove difficult to establish whether the impairment is due to AD pathology or to causes with alternate pathological substrates [37].

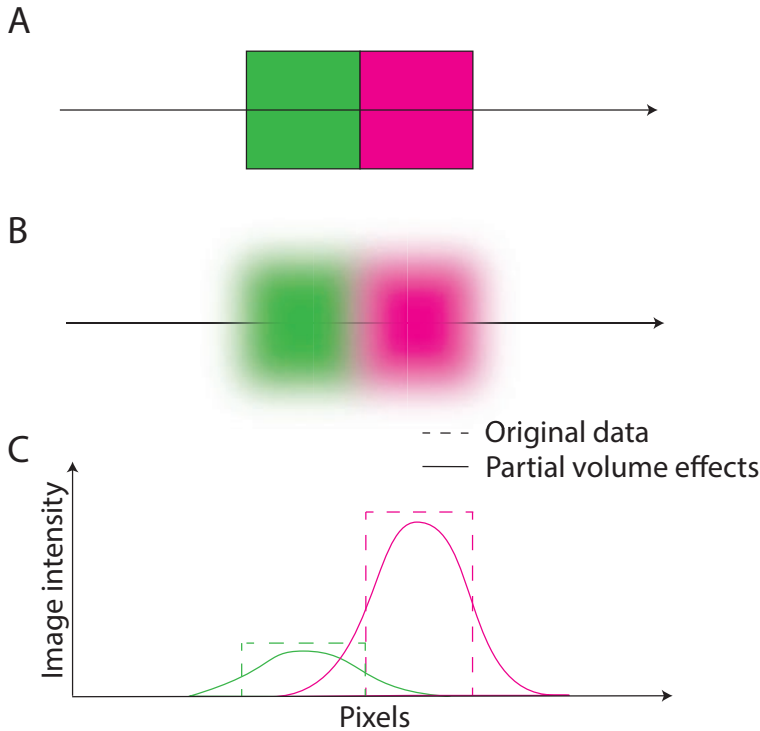


Figure 3. Schematic illustration of the impact of PVE on pixel data. A) Two adjacent structures of different radioactivity concentrations in the true data. B) Due to PVE, the intensity of each of the two structures spills out into the surrounding, resulting in a dilution of the intensity as shown in C). The impact of PVE results in a lower measured image intensity in the data subject to PVE than in the original data along the axes in A and B, but with a wider spread and an overlap between the two structures.

Clinical diagnosis of AD

Criteria for the clinical diagnosis of AD were first established in 1984 by the National Institute of Neurological and Communicative Disorders and Stroke and the Alzheimer's Disease and Related Disorders Association (NINCDS-ADRDA). It was then assumed that the clinical and neuropathological features of AD were invariably related in a one-to-one manner, such that an individual with dementia due to AD was assumed to have the underlying pathology [38]. The original clinical criteria stratified the diagnosis into probable AD (pAD) and possible AD based on clinical assessments and neuropsychological testing, with definite AD requiring histopathological confirmation from autopsy or biopsy together with a clinical diagnosis of pAD. Relative to autopsy neuropathology, the NINCDS-ADRDA criteria have

been shown to possess a sensitivity ranging from 70.9 to 87.3% and a specificity ranging from 44.3 to 70.8% [39].

In spite of being widely adopted and undeniably useful, the NINCDS-ADRDA criteria were recently revised based on important progress made in the clinical and neuropathological characterization of AD, as well as in new methods for detection of AD pathophysiology *in vivo* using biomarkers including, but not limited to, PET. These revisions, detailed by the National Institute of Aging and Alzheimer’s Association (NIA-AA) working groups, reflected a new understanding of AD, in which neuropathology and resulting clinical phenomenology were no longer considered synonymous. Specifically, AD has been reconceptualized as a dynamic clinicobiological entity in which β -amyloid toxicity is thought to set in motion a sequence of dynamic changes - including the accumulation of hyperphosphorylated tau species and synaptic depletion - with these changes thought to precede the onset of clinical symptoms by a decade or more [40], see Figure 4. As such, three novel sets of NIA-AA diagnostic criteria were proposed for the clinical continuum of AD, comprising asymptomatic “pre-clinical” [41], prodromal MCI [42] and dementia phases [43]. Similar criteria have been proposed by the International Working Group for New Research Criteria for the Diagnosis for Alzheimer’s Disease (IWG), in form of the IWG and IWG-2 criteria [44-46].

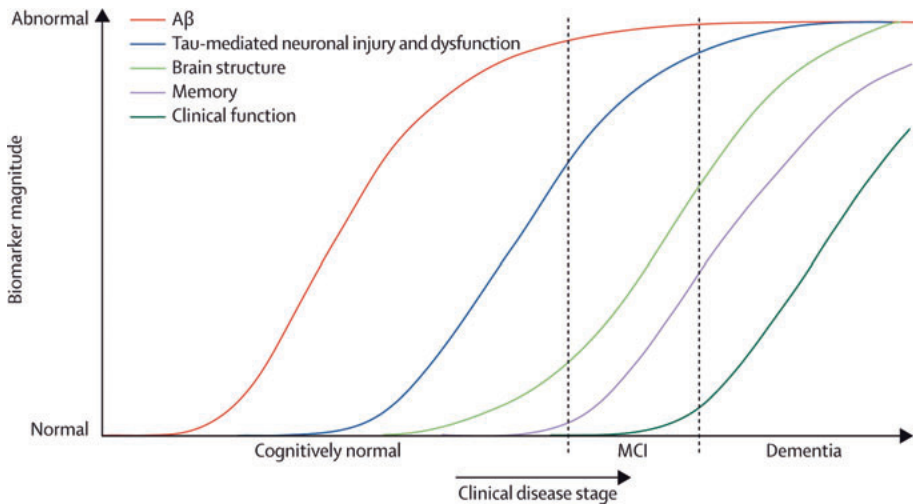


Figure 4. A hypothetical model of the dynamic biomarkers of the AD pathological cascade in relation to clinical disease stage, indicating that the β -amyloid ($A\beta$) accumulation precedes, and reaches a plateau before, the first appearance of clinical symptoms. Reprinted from Jack et al. [47] with permission.

Pathophysiology of AD

The neuropathology of AD is primarily manifested by two hallmarks: neurofibrillary tangles (NFTs) and senile plaques, both present in the first reported case of AD, as described by Alois Alzheimer in the beginning of the 20th century [48]. NFTs consist of deposits of fibrils of hyperphosphorylated tau in the neuronal perikarya [49]. The senile plaques are extracellular accumulations of β -amyloid, a cleavage product from the larger transmembrane protein amyloid precursor protein (APP) [50], which aggregates into insoluble fibrils in β -pleated sheet conformation, and are observed in two types, neuritic and the less dense diffuse plaques. The temporal spread of NFTs and neuritic plaques has been shown to follow characteristic patterns of propagation as a function of disease stage [51,52].

While the aetiology of the disease remains unclear, the identification of neuropathological hallmarks has been included in several sets of neuropathologic criteria for AD. These have been updated several times over the last decades, describing the frequency of neuritic plaques, leading up to a definition of probabilistic statements of the likelihood that the dementia demonstrated by a patient was caused by AD, rather than an absolute conclusion regarding the disease status [49,53-55].

For the neuropathological assessment of the presence and frequency of β -amyloid, several dyes are available for staining of the β -amyloid neuritic plaques, including Congo red, or the fluorochromes Thioflavin T or Thioflavin S for use with fluorescence microscopic methods [56]. The silver stain known as modified Bielschowsky silver stain (BSS) has also been shown to stain diffuse plaques [57].

Unlike the methods previously described, immunohistochemistry (IHC) can be used to provide a more quantitative estimate of the β -amyloid content of a tissue, giving an estimate of the percentage of a sample area containing β -amyloid deposits. The monoclonal antibody 4G8 can be used for this purpose and is specific for β -amyloid in contrast to BSS, which also stains NFTs [58].

AD and idiopathic normal pressure hydrocephalus

Patients with idiopathic normal pressure hydrocephalus (iNPH) exhibit enlarged ventricles due dysregulation of CSF. The clinical presentation is commonly described as a triad of clinical symptoms: cognitive impairment, gait abnormalities and urinary incontinence [59,60], with the main treatment ventriculoperitoneal shunt placement [61].

Patients with iNPH frequently exhibit comorbid AD pathology in the form of β -amyloid plaques [62,63], and patients where neuritic plaques are prevalent in brain biopsies taken during the shunt placement procedure also have more cognitive and gait impairment [64]. There are also indications

that the patient's response to the ventriculoperitoneal shunt may relate to whether the patient has AD pathology present, or inversely - the presence of AD pathology may work as an indication of the expected improvement from this invasive procedure [63-65].

β -amyloid PET imaging

The role of biomarkers has been central to the redefinition of AD, in particular the *in vivo* detection of β -amyloid using PET.

[^{11}C]Pittsburgh Compound B

About a decade ago, the first *in vivo* marker for β -amyloid deposition was developed, a PET tracer called [^{11}C]Pittsburgh Compound B ([^{11}C]PiB). It is a derivative of the histological dye Thioflavin T and binds to β -amyloid with high affinity. It was first studied with PET in 16 patients with AD and 9 healthy volunteers (HV), and was shown to have a two-fold higher tracer retention in the cortical regions of AD subjects than in HV subjects [66]. The binding of the tracer can be quantified by means of arterial input function kinetic modelling, using a reversible 2-TC, indicating a specific binding of the tracer [67]. SA of the uptake of [^{11}C]PiB indicated the presence of two main kinetic components, where the slower was related to V_T [67]. *In vitro* studies using AD brain tissue revealed that [^3H]PiB exhibits high and low affinity binding sites [68].

Simplified quantification can be done using the cerebellar cortex as a reference region due it being an area devoid of β -amyloid deposits until late in the course of AD. The reference tissue input can be used both for estimation of DVR based on dynamic data, as well as for estimation of SUVR in a static summation image over a shorter time window [69]. The optimal time window for such simplified scanning is 50-70 min post injection (p.i.) or 40-60 min if the dose is limited [70].

The characterization of [^{11}C]PiB tracer kinetics have been extensive, including validation of the use of parametric imaging from technical and clinical perspectives, showing that the visual assessment of BP_{ND} images may result in higher inter-reader and inter-method reliability than the use of static summation or SUVR images [71-73]. The *in vivo* binding properties of [^{11}C]PiB have been shown to correlate strongly with pathology measurements both in subjects who went on to autopsy [74-77] or in iNPH subjects that had a cortical biopsy taken during the shunt placement procedure [78]. No formal studies determining the sensitivity and specificity of [^{11}C]PiB in comparison with *post mortem* assessments of β -amyloid pathology have been conducted.

β -amyloid imaging in clinical research and practice

As the accumulation of β -amyloid is hypothesized to occur several years before the clinical onset of AD [79], a β -amyloid PET scan likely cannot follow the progression of AD. However, a negative scan is an important tool for ruling out AD as the underlying cause of cognitive impairment in a patient, and as a predictor of disease progression in patients with MCI [80]. While β -amyloid imaging using [^{11}C]PiB PET has been widely used and is considered a valid marker of β -amyloid deposition *in vivo*, its use as a diagnostic tool in clinical practice is limited by the short half-life of carbon-11 (20 min), which requires on-site production facilities and complex radiochemistry infrastructure. Fluorine-18, in contrast, has a half-life about 5.5 times longer than carbon-11 (110 min). As such, fluorine-18 labelled β -amyloid PET ligands allow for more centralized production and regional distribution and have therefore been developed and commercialized. To date, three such compounds have been approved for clinical use by U.S. and European regulatory bodies: the stilbenes [^{18}F]florbetapir ([^{18}F]AV-45; AmyvidTM) [81,82] and [^{18}F]florbetaben ([^{18}F]-BAY94-9172; NeuraceqTM) [83,84] and the Thioflavin T analogue [^{18}F]flutemetamol ([^{18}F]3'-F-PiB; VizamyTM) [85,86], which has recently also been approved in Japan and Korea. A fourth compound, [^{18}F]NAV-4694, formerly known as [^{18}F]AZD-4694, is currently under development [87,88].

The importance of β -amyloid imaging as a biomarker for AD was understood early on, leading to the formation of the Alzheimer's Disease Neuroimaging Initiative (ADNI) in 2004 [89], a research initiative collecting biomarker data from a large number of subjects and making all collected data openly available to the scientific community. Over a ten year period this initiative has resulted in over 600 scientific publications and contributed to the formation of the new diagnostic criteria for AD [90].

The increased insight in the presence of β -amyloid, thanks to the use of β -amyloid imaging, has revealed that the prevalence of β -amyloid pathology increases between 50 and 90 years of age from 10% to 44% in subjects without cognitive impairment [91]. A higher prevalence of β -amyloid accumulation has been seen in subjects carrying the apolipoprotein E genotype APOE- ϵ 4, representing the most important genetic risk factor for late-onset AD [92].

[^{18}F]Flutemetamol

[^{18}F]Flutemetamol, a 3'-fluoro-analogue of [^{11}C]PiB, was developed by GE Healthcare for commercialization together with the group that developed [^{11}C]PiB, and has been shown to exhibit similar properties as its parent compound, including a near identical inhibition constant K_i in human brain homogenate studies ([^3H]PiB K_i =1.9 nM, [^3H]flutemetamol K_i =2.4 nM) [93].

Molecular structures are shown in Figure 5. *Post mortem* binding studies in AD brain homogenates also showed a linear correlation between binding of [^3H]flutemetamol and [^3H]PiB ($r=0.99$), and a close correlation between the amount of bound [^3H]flutemetamol and β -amyloid content across 14 different brain regions ($r=0.92$) [93]. The first reported use of [^{18}F]flutemetamol *in vivo* was a dual tracer study, where two HV and one AD subject underwent [^{11}C]PiB and [^{18}F]flutemetamol scanning. The cortical retention characteristics of the two ligands were confirmed to match each other closely [94].

The first clinical trial of [^{18}F]flutemetamol, a Phase I study sponsored by GE Healthcare Ltd., was performed in Leuven, Belgium. This study was performed in two parts where the first aimed at investigating biodistribution and dosimetry in six HV. A good safety profile in terms of dosimetry was found, with a mean effective dose of $33.8 \pm 3.4 \mu\text{Sv/MBq}$, a level comparable to that of many other ^{18}F -labeled radiopharmaceuticals, where effective doses typically range from 20-35 $\mu\text{Sv/MBq}$ [95]. A similar dosimetry profile was also demonstrated in a Japanese cohort [96]. The second part of the Phase I study aimed at characterization of the binding properties in eight AD and eight HV, as well as validation of simplified methods for quantification [97]. The study showed that [^{18}F]flutemetamol binding was best described using a reversible 2-TC, and that brain uptake could be quantified using simplified methods and SUVR, using cerebellar cortex or pons as reference region, with high correlation to outcome parameters from compartment modelling ($R^2=0.95\text{--}0.98$). The optimal time window for simplified scanning was shown to be from 80 min and onwards, providing good separation between AD and HV, and sufficient count statistics.

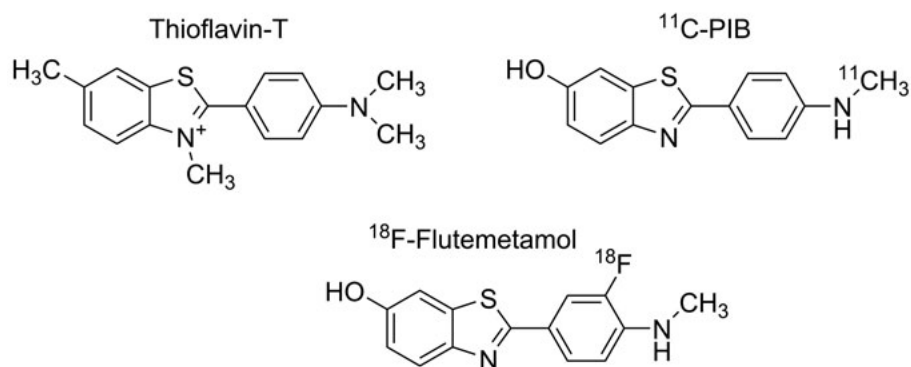


Figure 5. Molecular structures of the histochemical dye Thioflavin-T and its analogues carbon-11 labelled PiB and fluorine-18 labelled flutemetamol.

Quantification of [^{18}F]flutemetamol by means of SUVR has been found to be sensitive to PVE, but caution should be taken when applying corrections for PVE as the choice of method and characteristics of different anatomical regions could induce errors in the quantification [32].

The discriminating ability of late summation [^{18}F]flutemetamol scans (85-115 min p.i.) was confirmed in a Phase II multi-centre study including 25 HV, divided into 15 elderly (age > 55 years) and 10 young (age < 55 years), and 27 pAD subjects [98]. The PET images were assessed using both blinded visual assessment, with a methodology developed as part of the study, as well as quantitatively using SUVR. Examples of typical [^{18}F]flutemetamol negative (normal) and positive (abnormal) uptake patterns are shown in Figure 6.

The estimated sensitivity and specificity of visual assessment were 93.1% and 96.0%, respectively, when compared to the clinical diagnosis [98]. Two of the pAD subjects were rated as normal, and one of the elderly HV as abnormal, likely reflecting lack of specificity in clinical diagnosis and a case of pre-clinical AD. The test-retest variability of SUVR was determined to range from 1% to 4% in different regions in five subjects receiving two [^{18}F]flutemetamol scans. The efficacy of [^{18}F]flutemetamol visual assessments has also been investigated in 68 end-of-life patients using the *post mortem* diagnosis as standard of truth (SOT) [99]. The diagnosis was made

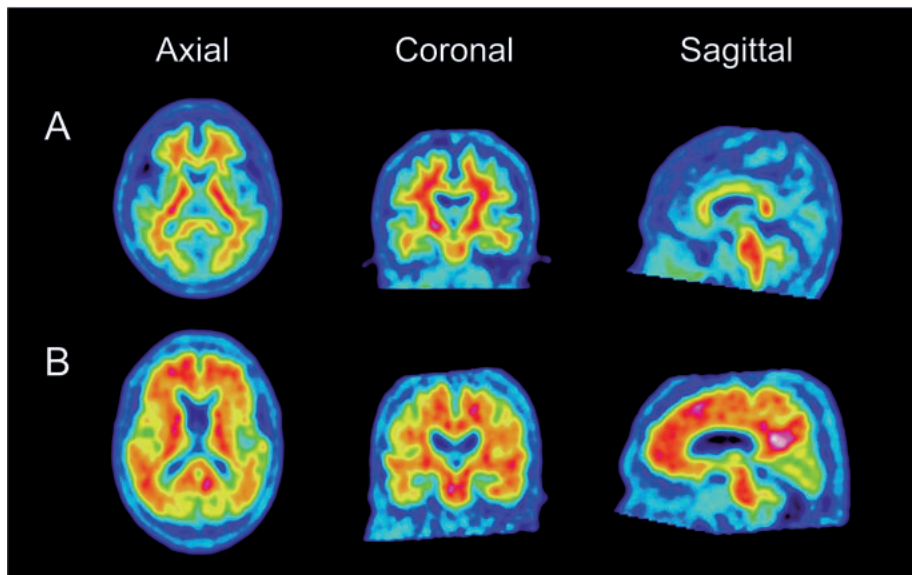


Figure 6. A) A subject with typical normal (“negative”) uptake with no evidence of β -amyloid accumulation show a high [^{18}F]flutemetamol uptake in the subcortical white matter and pons, but low uptake in the cortical regions. B) A subject with a typical abnormal (“positive”) uptake pattern, showing high uptake in the cortical regions.

based on the Consortium to Establish A Registry for Alzheimer's Disease (CERAD) pathology criteria [54], and the sensitivity of the visual assessment of five blinded readers ranged from 81% to 93%, with a median of 88%. The range of the specificity was somewhat wider, ranging from 44% to 92%, with a median of 88%. These numbers are comparable to those of the accuracy of the clinical diagnosis [39]. False outcomes were often associated with borderline neuritic plaque frequency according to the CERAD criteria, neuropathological evidence of DLB and severe brain atrophy [99].

[¹⁸F]flutemetamol in amnesic MCI

In addition to the pAD and HV subjects used to assess [¹⁸F]flutemetamol efficacy, the Phase II study also included 20 patients with the amnesic variant of MCI (aMCI), with 9 out of 11 classified as [¹⁸F]flutemetamol positive based on visual reads. A clinical follow-up was made in 19 of the 20 aMCI patients two years after the scanning showing that nine had progressed to pAD while ten retained the diagnosis of aMCI. Of the nine aMCI patients who had progressed to pAD, [¹⁸F]flutemetamol positivity was noted in seven, but in only one of the ten patients who had retained the diagnosis of aMCI at clinical follow up [100]. The use of [¹⁸F]flutemetamol to predict progression from aMCI to pAD using visual assessment has also been further investigated in 232 aMCI patients in a Phase III study. The median hazard ratio for progression among subjects with an abnormal visual rating was 2.58 (range: 1.96-3.42, $p=0.0001$) after a three-year clinical follow-up, meaning that within a three year period, an aMCI patient with a positive scan is about 2.6 times more likely to progress to pAD than an aMCI patient with a negative [¹⁸F]flutemetamol scan [101].

Comparison between [¹⁸F]flutemetamol and other β -amyloid ligands

Twenty pAD subjects and the 20 aMCI subjects underwent both a [¹⁸F]flutemetamol and a [¹¹C]PiB scan as part of the Phase II study. Although the two tracers differ in some aspects such as white matter retention, uptake values were found to correlate strongly across cortical regions ($r=0.83-0.92$) but not in pons and white matter ($r=0.22$ and $r=0.36$, respectively) [98]. The correlation between [¹⁸F]flutemetamol and [¹¹C]PiB was also investigated in a large dual tracer study performed in 166 Japanese subjects, confirming a high correlation between the SUVR of the two tracers ($r=0.96$) in cortical regions [102]. While no direct comparison has been made between [¹⁸F]flutemetamol and other fluorine-18 labelled β -amyloid ligands, comparisons with [¹¹C]PiB have been made for both [¹⁸F]florbetapir and [¹⁸F]florbetaben [103,104]. Using [¹¹C]PiB as a reference compound for all comparisons, [¹⁸F]flutemetamol was shown to have a comparable cortical uptake but higher white matter retention, whereas [¹⁸F]florbetapir had a lower cortical uptake than [¹¹C]PiB but no significantly higher white matter uptake [105]. [¹⁸F]Florbetaben has a lower cortical uptake and a higher white

matter uptake than [^{11}C]PiB [104]. The fourth fluorine-18 labelled β -amyloid ligand, [^{18}F]NAV-4694, has both a cortical and white matter uptake comparable to [^{11}C]PiB [106]. In spite of some differences in the regional uptake patterns of fluorine-18 labelled β -amyloid ligands, a review of the FDA Prescribing Informations [81,83,85] and EMA Summary Product Characteristics (SPC) [82,84,86] for the three approved tracers show that they can be expected to perform similarly in clinical settings, see Table 1.

Use of β -amyloid PET imaging ligands beyond AD

While the value of β -amyloid PET imaging may be greatest in the context of AD, findings from studies using [^{11}C]PiB suggest that [^{18}F]flutemetamol may also have value as marker of white matter pathology. As previously mentioned, the fluorine-18 labelled β -amyloid imaging tracers typically have a higher uptake in the subcortical white matter of the brain compared to [^{11}C]PiB in both HV and AD subjects, in spite of this tissue not being affected by β -amyloid pathology [52]. For [^{11}C]PiB, the uptake in white matter has been shown to be non-specific *in vitro* and *in vivo* [107]. The uptake has however also been hypothesized to be due to binding to the myelin basic protein, the major protein component of myelin, which assumes a β -pleated sheet conformation, similar to that of β -amyloid in senile plaques, in the presence of lipids [108,109].

Table 1. Clinical efficacy parameters of fluorine-18 β -amyloid PET tracers as stated in product labels by U.S. and EU regulatory authorities

| Regulatory authority and statistical measure | | [^{18}F]flutemetamol (Vizamyl TM) | [^{18}F]florbetapir (Amyvid TM) | [^{18}F]florbetaben (Neuraceq TM) |
|--|------------------------------------|--|--|--|
| FDA | Sensitivity (%); Median (range) | 93 (86-93) | 82 (69-92) | 96 (90-100) |
| FDA | Specificity (%); Median (range) | 84 (60-92) | 95 (90-95) | 77 (47-80) |
| FDA | Fleiss' kappa; Overall (95% CI) | 0.83 (0.79-0.86) | 0.83 (0.78-0.88) | 0.79 (0.77-0.83) |
| FDA | Intra-reader reproducibility (%)* | 93-100 | 91-100 | 91-98 |
| EMA | Sensitivity (%); Majority (95% CI) | 93 (81-99) | 92 (78-98) | 100 (80.5-100) |
| EMA | Specificity (%); Majority (95% CI) | 84 (64-96) | 100 (80-100) | 85.7 (67.4-100) |
| EMA | Fleiss' kappa; Range | - | 0.75-0.85 | 0.68-0.87 |

Abbreviations: FDA, U.S. Food and Drug Administration; EMA, European Medicines Agency; CI, Confidence Interval; * Intra-reader reproducibility was not included in the EMA SPC; - Fleiss' Kappa statistic (between-reader agreement) was not listed in the EMA SPC for [^{18}F]flutemetamol.

Recently, it was shown that the uptake of [^{11}C]PiB in white matter correlated with the mRNA expression of myelin proteins, as demonstrated when comparing voxel-wise DVR in an average image based on ten healthy subjects, with mRNA expression maps [110]. Changes in the uptake of [^{11}C]PiB in white matter lesions of patients with multiple sclerosis (MS), where the β -pleated sheet conformation is thought to be lost, has been demonstrated [108,111,112]. Further, studies have shown that β -amyloid imaging has a potential role in studying amyloidopathic disorders such as cerebral amyloid angiopathy (CAA) [113], cardiac amyloidosis [114,115], DLB [116] and Down's syndrome [117]. Deposition of β -amyloid has also been demonstrated in patients suffering from traumatic brain injury using [^{11}C]PiB [118], and may be useful in the prediction of clinical outcomes in iNPH patients undergoing shunt placement [65].

Summary

While the different approaches to quantification of PET studies all have their benefits and limitations, the multiple alternatives show the need for careful investigations as a new tracer is developed to validate that the indented parameter is correctly measured with the appropriate method. Though the use of [^{18}F]flutemetamol PET has gained an important role in AD, its application may extend to other diseases. The need for appropriate validation of the tracer binding is, regardless of its applied use, essential in order to realize the full potential of the ligand.

Aims of the thesis

The overarching aim of this thesis was to investigate the binding properties and quantification of [^{18}F]flutemetamol. This was done from two perspectives: the kinetic binding characteristics and the comparison and validation of [^{18}F]flutemetamol binding through neuropathology assessments.

Paper I

To investigate the performance of various methods for the creation of [^{18}F]flutemetamol parametric images representing the specific uptake of the tracer, using clinical data as well as testing the applicability of different kinetic models through simulation studies.

Paper II

To identify the kinetic components of [^{18}F]flutemetamol through SA, to investigate the impact of PVE on the kinetic modelling of [^{18}F]flutemetamol by means of simulations, and to develop methods for separation of tracer uptake due to binding to β -amyloid deposits and to binding in white matter.

Paper III

To investigate [^{18}F]flutemetamol brain uptake in Japanese elderly HV and clinically diagnosed pAD patients and to compare uptake in Japanese and Caucasian subjects.

Paper IV

To investigate the efficacy of [^{18}F]flutemetamol for *in vivo* detection of β -amyloid in the brain via the level of association between [^{18}F]flutemetamol and [^{11}C]PiB uptake and the degree of β -amyloid deposition in biopsy samples obtained from patients with iNPH.

Paper V

To investigate which estimates of [^{18}F]flutemetamol uptake and neuropathological SOT assessments correlate best, as determined in biopsy samples from iNPH patients, and whether quantitative [^{18}F]flutemetamol assessments are better at predicting pathology outcome than visual image assessments.

Paper VI

To compare [^{18}F]flutemetamol visual and quantitative assessments with the β -amyloid phase, neuritic plaque density and clinicopathologic status in 68 autopsy cases.

Materials and methods

Research participants

All studies were conducted in accordance with the Declaration of Helsinki, and approved by regional ethics committees whereby all participating subjects, or where applicable, their legal representatives, gave an informed consent for their participation.

Papers I and II were based on six Caucasian subjects recruited as part of the previously published Phase I study [97]. Three were elderly HV and three were clinically diagnosed as pAD. Paper III included eight elderly HV subjects and eight pAD of Japanese ethnicity, divided into two cohorts with different scanning protocols. Paper III also included a comparison with the subjects from the Caucasian Phase I study, including the six subjects from Papers I and II and an additional five elderly HV and five pAD, examined using a simplified scanning protocol as further detailed in the Study design section. The inclusion criteria for the HV subjects stated a Mini Mental State Examination (MMSE) score above 27 out of 30. The pAD subjects were required to fulfil the NINCDS-ADRDA criteria for pAD as well as the DSM-IV criteria for dementia of the Alzheimer's type. The inclusion criteria for pAD also stipulated an MMSE between 18 and 26, a Clinical Dementia Rating of 0.5, 1 or 2 and a Modified Hachinski Ischemia score ≤ 4 .

Paper IV included fifteen patients having previously undergone a 24 h intracranial pressure (ICP) monitoring and a brain biopsy due to suspected iNPH. The final clinical diagnosis of iNPH was based on all available clinical data and the 24 h ICP monitoring and AD or MCI diagnoses were based on the NIA-AA criteria.

Paper V is a pooled analysis of the study in Paper IV, and three additional studies of [^{18}F]flutemetamol in iNPH subjects, for a total of 50 patients. All patients in Papers IV and V were above the age of 50. In two of the studies included in the pooled analysis, [^{18}F]flutemetamol scanning was performed in subjects having already undergone the biopsy sample collection, for a total of 22 subjects. In the remaining two studies, including 28 subjects, [^{18}F]flutemetamol scanning was performed in patients with suspected iNPH before the shunt placement procedure and biopsy sample collection.

Paper VI included 68 subjects included in the previously published end-of-life clinical Phase III trial [99]. Dementia, defined according to the DSM-IV criteria, was noted as present or absent. Subjects were above the age of

55, terminally ill, and with a life expectancy of less than one year at the time of inclusion in the study.

Study design

Scanning procedures

Papers I, II and III focused on the kinetic characteristics and quantification of [^{18}F]flutemetamol, and studies performed in these subjects validated the use of a simplified scanning protocol and methods of quantification used in Papers IV, V and VI. Details of the scanning protocols are summarized in Figure 7. Subjects in Papers I and II underwent a dynamic PET scan together with arterial blood sampling used as input function in the kinetic modelling. The PET scans were acquired in list mode, and data were reconstructed into 25 frames with an increasing frame length (4×30, 3×60, 4×180, 8×300 s). Arterial blood samples for radioactivity measurements in whole blood and plasma were collected every 10 s during the first minute, every 15 s up until 3 min after injection and at 4, 8, 15, 30, 45, 60 and 90 min. In addition, arterial blood samples were collected at 2, 5, 20, 60, 180 and 240 min for determining the percentage of radioactive parent compound and metabolites.

In Paper III, Step A included three of the elderly HV and three pAD, who were scanned from the time of injection up to 150 min p.i. of [^{18}F]flutemetamol, with a break between 30 and 60 min p.i. when the participants were allowed to leave the scanner. The remaining five HV and five pAD were scanned from 80 min p.i., ending at 130 min p.i. (Step B). Data from the Japanese cohort was compared with that from the previously performed Caucasian Phase I study, however, the only shared scanning window for all 32 subjects was between 80-90 min p.i.

In Papers IV and V, [^{18}F]flutemetamol PET scans were performed over 30 min starting approximately 90 min p.i. Seven of the 15 subjects in Paper IV also underwent a dynamic [^{11}C]PiB scan with a duration of 90 min, starting at the time of injection. Static summation images for estimation of [^{11}C]PiB SUVR were limited to the time window between 40 and 70 min p.i.

The target dose of [^{18}F]flutemetamol was 185 MBq in all subjects in Papers I-V. In Paper VI, the scanning duration was limited to 10 min due to the condition of the end-of-life patients, and the target dose was increased to 370 MBq in order to increase count statistics to maintain image quality in spite of shorter scan duration. The maximum total amount of injected cold flutemetamol was 10 μg for the 185 MBq target dose, administered in the antecubital vein over approximately 40 s. The mean injected dose of [^{11}C]PiB in Paper IV was 473 MBq.

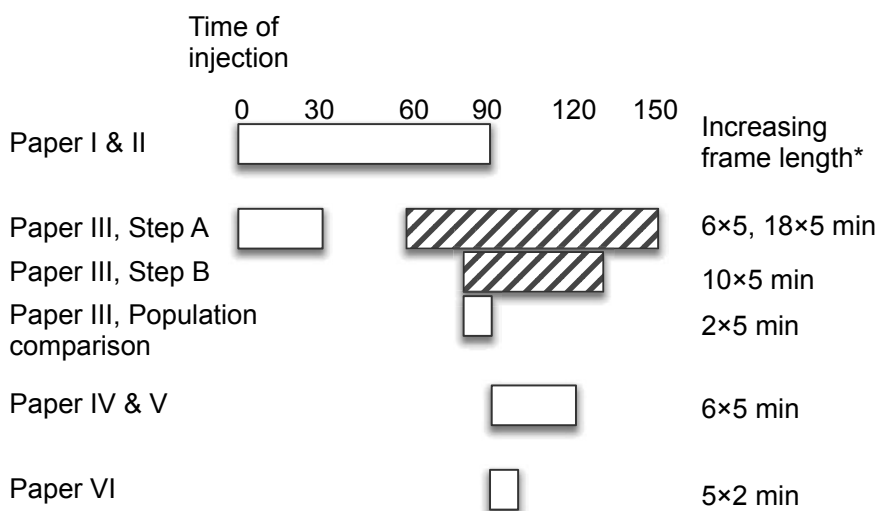


Figure 7. Overview of scanning protocols throughout the included papers.

* Scanning in Papers I and II were performed with increasing frame length: 4x30, 3x60, 4x180, 8x300 s.

Subjects in Papers I-V also underwent a structural T1 MRI used for VOI definition and to exclude subjects with anatomical abnormalities. Most end-of-life patients included in Paper VI were not able to undertake an MRI, but all subjects were scanned on PET/CT scanners, providing a high-quality CT for VOI definition. Those iNPH subjects in Paper V that had their shunt placement procedure after [^{18}F]flutemetamol scanning also underwent a post-surgery CT in order to enable correct positioning of VOIs corresponding to the biopsy sample location.

Papers I-IV were single centre studies while Paper V was a pooled analysis of four single centre studies. Paper VI was a multi-centre study with imaging performed at 12 imaging sites. All scanners were qualified prior to study start, and optimal reconstruction settings for each imaging site, including corrections for attenuation, random counts and scatter, were determined using phantom scanning. Most sites used iterative 2D reconstruction with a Gaussian post-reconstruction filter, resulting in a uniform spatial resolution of 5-7 mm FWHM.

Radiochemistry

The investigational product [^{18}F]flutemetamol was manufactured according to both good manufacturing practice and GE Healthcare procedures at TracerLab-FX (Papers I and II) or FASTlab chemistry platforms (Papers III-VI) and tested for chemical and radiochemical purity using high-performance liquid chromatography. The [^{11}C]PiB injections used in Paper IV were man-

ufactured according to local procedures and good manufacturing practice at Turku PET Centre, Turku, Finland.

Tissue analysis

Biopsy procedures

The biopsy samples used in Papers IV and V were taken using a biopsy forceps or a 14-gauge biopsy needle from the site of insertion of the intraventricular catheter. The site of biopsy sampling was either the right prefrontal or parietal cortex, in keeping with local neurosurgical procedures.

The biopsy samples were fixed in formalin and embedded in paraffin and divided into up to 50 serial sections, 5 or 6 μm thick, depending on the sample size. Tissue sections were assessed using three staining techniques: 4G8 IHC (Prod No. SIG-39220, Covance, USA) for the automated determination of the percentage area of β -amyloid in grey matter, and semi-quantitative histochemical (HC) assessment using Thioflavin S and BSS. Using the latter two assessments, plaques were counted and scored by independent neuropathologists blinded to all other data, using a modification of the CERAD criteria 4-point scale with the scoring of 0 = no plaques, 1 = sparse plaques (1 to 5 plaques), 2 = moderate plaques (6 to 19) and 3 = frequent plaques (≥ 20). Thioflavin S and BSS were dichotomized into normal and abnormal, where a score of 2 and 3 were considered abnormal. In Paper V, 4G8 assessments were also dichotomized using a cut-off of 2.5%. In one of the studies included in the pooled analysis in Paper V, Thioflavin S and BSS were assessed using a different scale, and the samples of the 7 subjects included in this study were therefore not part of the pooled analysis. The time between biopsy and PET procedure in the studies where biopsy had been performed prior to [^{18}F]flutemetamol scanning ranged from 3 to 45 months, and approximately 3-8 weeks in the studies where the [^{18}F]flutemetamol scan was performed before the biopsy.

Autopsy procedures

Brains were collected *post mortem*, fixed in formalin and cut in coronal slices. Paraffin sections 5 μm in thickness were then taken from frontal, parietal, temporal, and occipital cortices, as well as the entorhinal cortex, hippocampus, basal ganglia, thalamus, amygdala, midbrain, pons, medulla oblongata and cerebellar tissue blocks, and assessed using 4G8 IHC (Prod No. SIG-39220; Covance, USA) and BSS. The sections were also assessed for other pathological hallmarks, including hematoxylin and eosin staining for general neuropathological assessment, abnormal phosphorylated tau using AT8 IHC (Prod No. MN1020, Thermo Scientific, UK), α -synuclein IHC (Prod No.

NCL-L_ASYN, Leica Biosystems, UK) and ubiquitin IHC (Prod No. Z0458, DakoCytomation, UK). This enabled the classification of subjects into diagnoses such as DLB, CAA, and tauopathies e.g. frontotemporal lobar degeneration with tau inclusions (FTLD-tau) including progressive supranuclear palsy and Pick’s disease, in addition to AD.

Staging of β -amyloid pathology was determined as follows: phase 0 = none, phase 1 = deposition of β -amyloid exclusively in the neocortex, phase 2 = deposition additionally in the allocortex, phase 3 = deposition additionally in diencephalon, phase 4 = deposition additionally in the brainstem and phase 5 = deposition additionally in the cerebellum [52,119]. In 32 subjects, the percentage area of β -amyloid in grey matter was determined using 4G8.

Subjects were also assessed based on the stage of NFT pathology [51], with a neuropathological diagnosis of AD performed according to the NIA-AA guidelines [120]. The scan to death interval ranged between 0 and 397 days, with a median of 78 days.

Efficacy analysis

Using pathology assessment as SOT, each subject in Papers IV and V was classified into one of the following: true positive (TP), false negative (FN), true negative (TN) or false positive (FP) as described in Table 2. The diagnostic efficacy parameters sensitivity, specificity, accuracy, positive predictive value (PPV) and negative predictive value (NPV) for [^{18}F]flutemetamol were then estimated using these classifications, as described in Table 3.

Table 2. Classification scheme of subjects using pathology as standard of truth

| $[^{18}\text{F}]$ flutemetamol PET outcome | Pathology standard of truth | |
|--|-----------------------------|---------------------|
| | Abnormal | Normal |
| Abnormal | True positive (TP) | False positive (FP) |
| Normal | False negative (FN) | True negative (TN) |

Table 3. Definitions of diagnostic efficacy parameters

| Metric | Definition |
|---------------------------------|---|
| Sensitivity | $\text{TP} / (\text{TP} + \text{FN})$ |
| Specificity | $\text{TN} / (\text{TN} + \text{FP})$ |
| Accuracy | $(\text{TP} + \text{TN}) / (\text{TP} + \text{FN} + \text{TN} + \text{FP})$ |
| Positive predictive value (PPV) | $\text{TP} / (\text{TP} + \text{FP})$ |
| Negative predictive value (NPV) | $\text{TN} / (\text{TN} + \text{FN})$ |

Clinicopathologic classification of end-of-life patients

As part of Paper VI, end-of-life patients were classified according to their cognitive status at the time of inclusion combined with the neuropathological assessment:

- *Symptomatic AD*: demented patients with at least intermediate AD pathology according to the NIA-AA criteria
- *AD-type mixed dementia*: patients with dementia where other dementia-related pathology were apparent together with intermediate or high degrees of AD pathology according to the NIA-AA criteria
- *Non-AD dementia*: patients with dementia but without intermediate or high degrees of AD pathology according to the NIA-AA criteria, including patients with vascular dementia, DLB and FTLT-tau
- *p-pre-AD*: non-demented patients with AD pathology
- *Non-AD controls*: no AD pathology and non-demented

Image data analysis

Image processing

The first step of the image processing, consistent throughout all included papers, was to correct for subject movement during the scan using a rigid frame-to-frame realignment procedure [121] performed in VOIager, version 2.0.5 (Papers IV, V and VI) or version 4 (Papers I, II and III) (GE Healthcare Ltd., Uppsala, Sweden).

In Papers I and II, PET and MRI were co-registered by means of an early summation image of frames 2-10 using Statistical Parametric Mapping (SPM5; Wellcome Trust Center for Neuroimaging, University College of London, London, UK).

The MRI data in Papers III, IV and V were manually realigned in order to resample the data to have the transverse planes parallel with the line connecting the anterior and posterior commissure. Dynamic data of Paper III and summation PET images, for all [^{18}F]flutemetamol frames and 40-70 min for [^{11}C]PiB, in Papers IV and V were then co-registered to the realigned MRI. The purpose of the manual realignment was to achieve a uniform orientation of all images for the blinded visual image assessment of images in Papers IV and V, further described below, and to achieve an optimized starting point for spatial normalization. Anatomical images in Papers III-VI were spatially normalized to the Montreal Neurological Institute (MNI) MRI T1 template using a polynomial non-linear registration, and transformation parameters were also applied to the co-registered PET data, to allow for application of a predefined VOI template in standard space [122].

For quantification purposes the previously described steps were performed also for data in Paper VI. However, realignment of image data for the visual assessment was performed as part of the assessment.

Blinded visual image assessments

Visual assessments of the summation data included in Papers IV and V were performed by three experienced nuclear physicians blinded to clinical and pathological information, after having undergone training of the read methodology with an instructor.

In Paper VI, involving end-of-life patients, five nuclear medicine physicians or radiologists with no previous experience of β -amyloid PET imaging underwent training for visual assessments by means of an electronic training program. The readers were blinded to all clinical and pathological information and rated the images as normal or abnormal with respect to [^{18}F]flutemetamol uptake, as a proxy for β -amyloid status, together with the CT of each subject. Prior to the read, the PET and CT images were realigned into a plane where the transversal slices were approximately parallel to the line connecting the anterior and posterior commissure by external nuclear medicine technicians, also trained with the electronic training program on how to identify the correct orientation.

All visual assessments were performed centrally on Xeleris workstations (GE Healthcare Medical Systems, Milwaukee, USA). All images were rated as normal or abnormal with respect to [^{18}F]flutemetamol grey matter uptake pattern.

VOI definitions

Probabilistic grey matter segmented VOIs

In Papers I and II, VOIs were defined based on a segmentation of grey and white matter using a dedicated software, PVElab [33]. This software transforms a VOI template into patient space through a non-rigid transformation and uses MRI information to segment the VOIs into grey and white matter. Cerebellar cortex was included for validation as reference region in both Papers I and II as well as sixteen grey matter regions averaged across the two hemispheres: superior frontal cortex, medial inferior frontal cortex, orbitofrontal cortex, dorsolateral prefrontal cortex, ventrolateral prefrontal cortex, superior temporal cortex, medial inferior temporal cortex, insula, parietal cortex, thalamus, sensory motor cortex, putamen, caudate, anterior cingulate and posterior cingulate. Examples of PVElab MRI-segmented VOIs are shown in Figure 8 A. In Paper II, all grey matter regions of the template were combined into one large VOI, and compared to the total white matter as defined by the segmentation.

VOIs could then be applied to the dynamic PET data for extraction of TACs used in the regional kinetic modelling, or to parametric images providing an average parameter estimate of the voxels included.

MNI template space VOIs

In Papers III-VI, a pre-defined template of VOIs in MNI space was used, including five cortical VOIs covering anatomical regions known to be affected by β -amyloid accumulation in AD: prefrontal cortex, anterior cingulate, lateral temporal cortex, parietal cortex and precuneus plus posterior cingulate, shown in Figure 8 B.

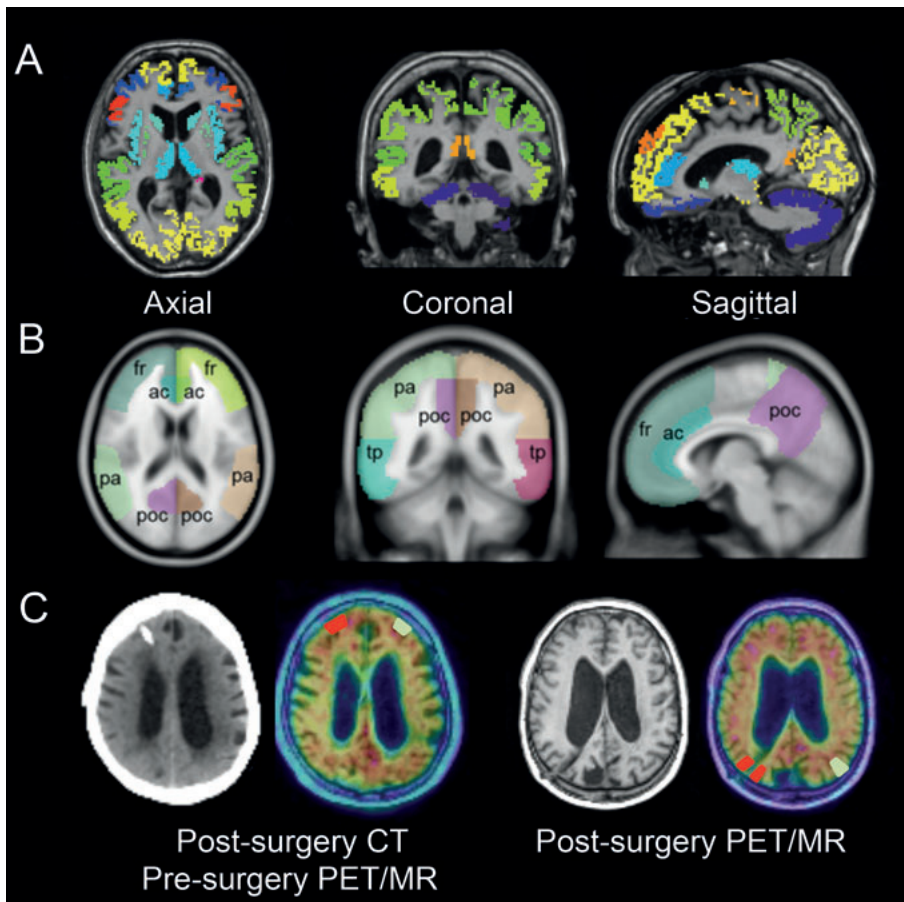


Figure 8. A) MRI segmented grey matter VOIs from PVELab. B) MNI template space VOIs, fr = frontal cortex, ac = anterior cingulate, pa = parietal cortex, poc = posterior cingulate and precuneus, tp = lateral temporal cortex. C) Left: Post-surgery CT and pre-surgery PET/MRI overlay with biopsy VOIs as outlined in patients having [^{18}F]flutemetamol scan performed before the shunt placement procedure. Right: Post-surgery MRI and PET/MRI overlay with biopsy VOIs as outlined in patients having [^{18}F]flutemetamol scan performed after the shunt placement procedure.

Paper III also included analysis of medial temporal cortex, sensory motor cortex, occipital cortex, striatum and the subcortical white matter. Cerebellar cortex was used as reference region, but pons was also included as an alternative reference region. In biopsy and end-of-life patients, VOIs were manually adjusted for atrophy and, in the case of iNPH subjects that had an inserted intraventricular shunt at the time of PET scanning, for the shunt itself. In addition to the separate anatomical VOIs, a global estimate was achieved by combining prefrontal cortex, anterior cingulate, lateral temporal cortex, parietal cortex, precuneus and posterior cingulate into one VOI, called the composite VOI.

VOIs were applied to the dynamic data part of Paper III, for extraction of TACs used in kinetic modelling, or to summation images in Papers IV-VI for estimation of SUVR.

Biopsy VOIs

For definition of VOIs corresponding to the biopsy sample collected in Papers IV and V, the image data were reoriented so that the VOIs could be defined in plane with the shunt. In those subjects where [^{18}F]flutemetamol and MRI were performed after the shunt placement, a VOI was defined surrounding the sampled area, i.e. surrounding the shunt. In subjects undergoing [^{18}F]flutemetamol scanning and MRI prior to shunt placement, the post-surgery CT was used to locate the biopsy sampling area and the VOI defined on the exact location. In addition to the ipsilateral VOI corresponding to the sampling location, a VOI in the matching location on the contralateral side was defined in all subjects. Illustrations of the outlining of biopsy VOIs are shown in Figure 8 C.

Partial volume effects correction

In addition to VOI definition, PVElab was also used for correction of PVE in Paper II, where the effect of PVE on the quantification of tracer uptake was investigated. TAC data was corrected using the modified Müller-Gärtner method [28].

Kinetic modelling

In Papers I and II where arterial blood sampling had been performed, a 2-TC [9] was used for estimation of the tracer binding through non-linear least squares curve fitting, using a metabolite-corrected plasma input function. The appropriateness of this model in describing the tracer uptake had previously been demonstrated [97]. BP_{ND} for each region was estimated both directly and indirectly as DVR-1 [14]. The compartment model-based binding estimates were considered the gold standard and the other models were compared against them. Clearance rates estimated from 2-TC were used to con-

firm the validity of the basis functions used in the parametric models. VOI-based analysis was also performed using SRTM [14]. In Paper III, the application of SUVR in Japanese subjects was investigated and validated against reference Logan DVR-1, fitting over 60-150 min [19]. All kinetic modelling was performed using in-house developed MATLAB (The Mathworks Inc., Natick, USA) implementations of published and referenced methods.

Spectral analysis

The kinetic components of [^{18}F]flutemetamol uptake in grey matter, white matter and cerebellar cortex were identified using SA with and without correction for PVE. Fifty basis functions were used with predetermined β , logarithmically distributed between 0.0111 and 2 min^{-1} , returning the peak height α_i . The lower boundary is equal to $1/T$ where T is the scanning duration of 90 min [24]. The basis functions were divided into kinetic components based on clusters in the peak distribution across all subjects. The volume of distribution for each component was estimated as $V_j = \sum \alpha_i / \beta_i$, i.e. the sum of each of the i basis functions within the component, as well as the percentage contribution of each V_j to the total V_T ($\%V_j$). Differences in grey and white matter properties were identified in the six subjects divided based on uptake pattern, and used as a method for potential discrimination of uptake type in the creation of parametric images.

Parametric images

Parametric maps studied in Paper I were generated using in-house developed MATLAB based implementations of the following models: three multilinear reference tissue models (MRTMo, MRTM and MRTM2) [20,21], RPM [14,26] and RPM2 [18], as well as voxel-based reference Logan over 50-90 min [19]. A voxel-based representation of SUVR was also created for the summation image over 70-90 minutes. Cerebellar grey matter was used as reference region in all models.

For RPM and RPM2, 50 basis functions with logarithmically spaced clearance rates ranging between 0.012 and 0.6 min^{-1} were used. These boundaries were compared to the clearance rates estimated during the VOI-based 2-TC analysis of all subjects.

As the target-to-reference region ratio could not be assumed to be constant during the time window studied, the k_2' for the cerebellar cortex VOI was determined graphically using plasma input Logan. Parametric reference Logan images were created with and without inclusion of the k_2' to assess the impact of this correction [19]. The included k_2' was either individually determined or based on the cohort mean.

Due to the sensitivity of parametric methods to noise, in graphical analyses especially [13], an isotropic Gaussian filter of 5 mm was applied to the

dynamic reconstructed data before estimation of parametric images and compared to no additional smoothing [123]. No additional pre-filter was applied to SUVR, as it does not suffer from noise impact on model fitting in the same way as the parametric models. VOIs were applied to the parametric images and the results compared with 2-TC estimates.

As part of Paper II, parametric images were created using voxel-based SA with five basis functions, with β logarithmically distributed between 0.0111 and 2 min⁻¹. VOIs were applied to the parametric SA images and the results compared with VOI SA estimates. Following the definition of the unique properties of grey matter and white matter as identified by the VOI-based SA, voxels were classified as typical grey matter or white matter and two parametric images for each subject were created, one including only the voxels classified as grey matter and one including only voxels classified as white matter. For each unique voxel, V_T was estimated in each respective parametric image. In addition, parametric images were created containing only the component hypothesized to be specific for the binding to β -amyloid in grey matter: one parametric image containing all voxels, and one containing only voxels classified as grey matter.

Simulation studies

The validity of different kinetic models in the estimation of [¹⁸F]flutemetamol was tested through simulations, where TACs were generated for target and reference regions representing typical [¹⁸F]flutemetamol kinetics using a typical plasma input curve and the plasma input reversible 2-TC [9]. Parameter values were based on the clinical data. A noise level of 2% or 10%, corresponding to noise levels present in VOI TACs or single voxel TACs, was added to the simulated target signal, whereas a noise level of 2% was added to the simulated reference region TAC. The models tested were the 2-TC estimation of BP_{ND} , directly and as DVR-1, a curve fitting model (SRTM), a graphical model (reference Logan) and a basis function model (RPM). One hundred TACs with added noise were generated, and the bias and coefficient of variation (CoV), representing the accuracy and precision of BP_{ND} and/or DVR-1, were used for evaluation. In addition to this, simulated SUVR was estimated for the time interval 70-90 min. To test the correlation between true BP_{ND} or DVR-1 and the different simplifications, 100 different BP_{ND} and DVR-1 levels randomly chosen between 0.38 and 1.14 were simulated and the coefficient of determination (R^2) and slope between the different binding estimates were computed.

The impact of PVE on the quantification of [¹⁸F]flutemetamol uptake by means of SA was investigated through simulations. Digital phantom scans were created by using grey/white matter segmented MR images from one representative [¹⁸F]flutemetamol negative and one positive subject, assuming homogenous tracer uptake within grey matter, white matter and cerebellar

cortex. Characteristics of tracer uptake were based on plasma input functions and kinetic parameters of the three tissue types from SA as performed in the two subjects. PVE were simulated by applying smoothing using a Gaussian point spread function of 7 mm FWHM on the digital phantom, achieving a similar level of spatial resolution as the experimental data. TACs were generated for the original and smoothed digital phantom and quantified using SA as previously described. The recovery was estimated through comparison of the radioactivity concentration in each tissue type before and after smoothing and the effects of PVE on the digital phantoms were assessed by comparison of the original and smoothed data.

Statistical analyses

Paper I

Performance of the various parametric methods was determined based on comparisons with VOI-based 2-TC estimates as the gold standard, providing an estimate of the strength of the relationship between the two using the coefficient of determination (R^2), slope and intercept. Accuracy and precision of different models were estimated through simulations with CoV and bias as outcome, compared to 2-TC as gold standard.

Paper II

The validity of the application of SA to [^{18}F]flutemetamol data was assessed through comparisons with VOI-based 2-TC as gold standard. The application of a voxel-based SA was then correlated to VOI-based SA. Both analyses were done using Pearson's correlation coefficient (r) as an estimate of the associational strength. Effects of PVE correction were assessed using Student's t-test, with a p-value < 0.05 considered statistically significant.

Paper III

The relationship between reference Logan estimated DVR and SUVR were evaluated using Pearson's correlation coefficient (r) as an indicator of the strength of the association. Differences in regional SUVR between HV and pAD, and between populations, were evaluated using a Student's t test, with a p-value < 0.05 considered statistically significant.

Paper IV

Pearson's correlation coefficient (r) was used as an estimate of the strength of the correlation between [^{18}F]flutemetamol SUVR in the ipsilateral, contralateral and composite VOI vs. 4G8 estimated β -amyloid percentage area and for the correlation between [^{18}F]flutemetamol and [^{11}C]PiB ($p < 0.05$ considered statistically significant). A regression model analysis including time

between biopsy and PET scan was also performed. Visual assessment of [^{18}F]flutemetamol data was compared to dichotomized pathology assessments (BSS, Thioflavin S and overall pathology assessment) for the majority outcome of the visual read, and efficacy parameters were calculated.

Paper V

Four different SOTs were defined (4G8 percentage area, BSS, Thioflavin S and overall pathology) and compared to six types of quantitative estimates of [^{18}F]flutemetamol uptake (ipsilateral, contralateral and composite SUVR using cerebellar cortex (SUVR_{CER}) or pons ($\text{SUVR}_{\text{PONS}}$) as reference region), resulting in 24 pairs of SOT vs. [^{18}F]flutemetamol uptake. Receiver operating characteristic (ROC) analyses were performed for each pair. Based on the Youden index, the optimal threshold for SUVR dichotomization was determined and using that threshold, the efficacy parameters were estimated for each pair.

The performance of visual assessments vs. quantitative assessments of [^{18}F]flutemetamol was investigated using the McNemar test and the sum of sensitivity and specificity as a measurement of overall performance.

Paper VI

A logistic regression model, controlling for age, sex and scan-death interval was used to investigate the influence of β -amyloid phase and NFT stage on [^{18}F]flutemetamol visual assessment outcome. The correlation between the 4G8 estimated β -amyloid percentage area and composite SUVR was assessed using Pearson's correlation coefficient (r) as outcome. A binary logistic regression model, also controlling for age, sex and scan-death interval, was used to investigate the relationship between visual assessments and the clinicopathologic classification. Analysis of variance (ANOVA) was used to study the impact of β -amyloid phase and clinicopathologic classification on [^{18}F]flutemetamol SUVR, corrected for multiple testing using Games-Howell post hoc test. Ability to distinguish p-pre-AD from non-demented control subjects based on visual assessments was investigated using Fischer's exact test, and based on SUVR using ANOVA.

Results

Kinetic properties of [^{18}F]flutemetamol

Basic quantification of [^{18}F]flutemetamol uptake

The kinetics of [^{18}F]flutemetamol were well described by the 2-TC, using both direct and indirect estimation (DVR-1) of BP_{ND} . Summation images and the estimated BP_{ND} in the orbitofrontal cortex for the six subjects included in Papers I and II are shown in Figure 9. According to the Akaike information criterion, SRTM resulted in the best fits to experimental data. The correlation with the 2-TC estimates, however, was low.

In Step A of Paper III, SUVR over 85-115 min showed a high correlation with DVR estimated using cerebellar reference-based Logan applied to the 60-150 minute time window (Pearson's $r = 0.97$).

Group comparisons

The discriminating abilities of [^{18}F]flutemetamol PET were investigated by pooling all Japanese subjects from Step A and Step B in Paper III. Visually, the images showed an increased level of intensity in cortical regions for the pAD subjects compared to the HV subjects, except in three pAD subjects from the Step B cohort, which had a typical negative uptake pattern. SUVR for the time window 85-115 min was significantly raised in nearly all of the cortical areas in the pAD subjects compared with HV subjects, except in the medial temporal cortex ($p = 0.426$). The striatal and composite SUVR were also significantly raised in pAD ($p = 0.001$ and $p = 0.002$, respectively) whereas pons and subcortical white matter SUVR were not ($p = 0.392$ and $p = 0.167$, respectively).

Population based analysis

There were no significant differences comparing SUVR over 80-90 min between Japanese and Caucasian HV or Japanese and Caucasian pAD, (p -value range: 0.07 - 0.88), after exclusion of pAD subjects with negative uptake pattern and one Caucasian HV with a positive uptake pattern.

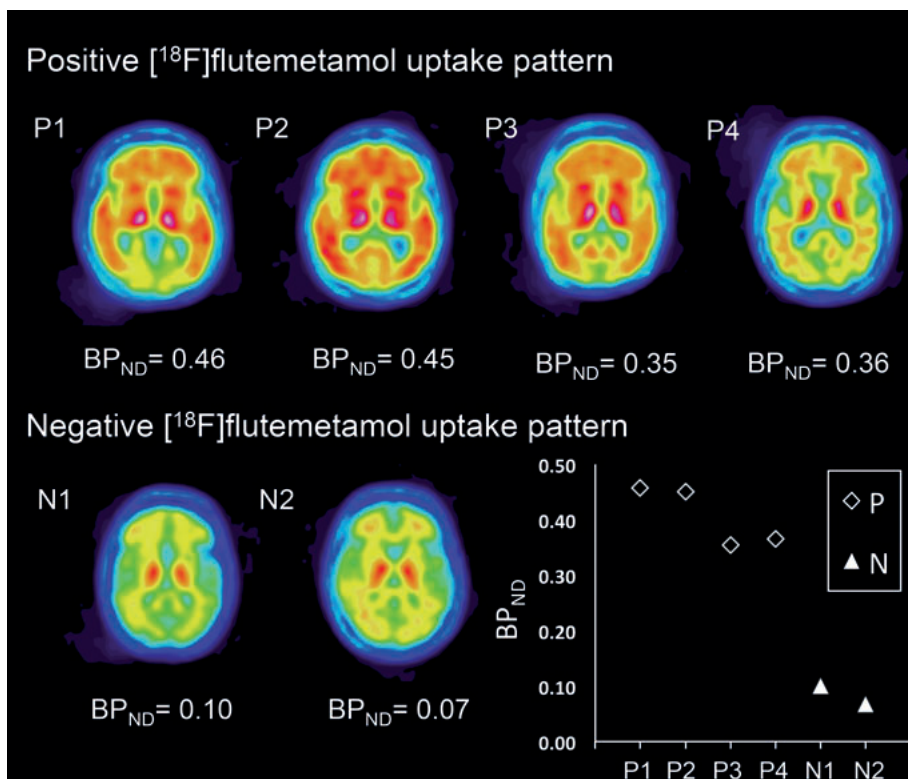


Figure 9. Summation images of the six subjects included in Papers I and II. Subjects P1-P3 had a clinical diagnosis of pAD, whereas subjects P4, N1 and N2 were cognitively normal HV subjects. The graph in the lower right corner shows the BP_{ND} of the orbitofrontal cortex for all subjects, estimated with 2-TC. Diamonds (\diamond) indicate subjects with $[^{18}\text{F}]$ flutemetamol positive uptake pattern and triangles (\triangle) subjects with a $[^{18}\text{F}]$ flutemetamol negative uptake pattern.

Comparison between $[^{18}\text{F}]$ flutemetamol and $[^{11}\text{C}]$ PiB

Seven patients in Paper IV underwent both a $[^{18}\text{F}]$ flutemetamol and a $[^{11}\text{C}]$ PiB scan. A significant correlation was found between $[^{18}\text{F}]$ flutemetamol and $[^{11}\text{C}]$ PiB SUVR in the composite VOI as well as in VOIs ipsilateral and contralateral to the biopsy site (Pearson's $r = 0.97$, $r = 0.83$ and $r = 0.92$, respectively).

Spectral analysis for characterization of tracer binding

SA estimates of DVR-1 in 16 grey matter VOIs, using cerebellar cortex as reference region without correction for PVE, correlated well with 2-TC DVR-1 estimates (Pearson's $r = 0.98$, slope = 1.04).

Three main categories of kinetic components were identified in the uptake of $[^{18}\text{F}]$ flutemetamol using SA, both in negative ($n = 2$) and positive subjects ($n = 4$). The categories were defined, ranging from slow to fast, as A: $\beta \leq$

0.0111 min⁻¹, B: β ranging from 0.0124 to 0.1748 min⁻¹ and C: β ranging from 0.267 to 2 min⁻¹, with V_A , V_B and V_C being the volume of distribution of each component.

The contribution of the components to V_T in the data corrected for PVE did not differ between the negative and positive subjects in cerebellar cortex or white matter. In the cerebellum, component A was not detected while component B was dominant ($\%V_B = 97.7\% \pm 1.1$). In contrast, component A was dominant in white matter ($\%V_A = 90.0\% \pm 4.4$), followed by component B ($\%V_B = 9.6\% \pm 4.2$).

Component A was absent in the grey matter of the two [¹⁸F]flutemetamol negative subjects, and approximately 100% of V_T was from component B, similar to cerebellar cortex. In three of the four [¹⁸F]flutemetamol positive subjects, however, $\%V_A$ in grey matter varied between 21 and 42%, whereas component A was absent in the fourth positive subject. The contribution of component C was negligible in all tissue types.

Impact of partial volume effects

Correction of [¹⁸F]flutemetamol uptake for PVE resulted in an increase of V_T in cerebellar cortex by $14\% \pm 0.4$ ($p < 0.001$), but did not affect the relative contribution of the different components; also without PVE correction component B represented the entire V_T . PVE correction had no significant effect on V_T in white matter, however $\%V_A$ increased ($p < 0.001$) and $\%V_B$ decreased ($p < 0.001$) compared to uncorrected data. No significant change in V_T was observed in grey matter either, however $\%V_A$ decreased (and was removed completely in two subjects, $p = 0.03$) while $\%V_B$ increased ($p = 0.03$), opposite to the effect in white matter.

Discrimination of tissue types

A threshold for discrimination of grey and white matter was defined as the midpoint between white matter and grey matter average contribution of component A. This was expressed as the number of standard deviations of $\%V_A$ in data uncorrected for PVE in grey and white matter:

$$\text{Threshold} = \overline{\%V_A^{WM}} - \frac{\overline{\%V_A^{WM}} - \overline{\%V_A^{GM}}}{SD^{WM} + SD^{GM}} \cdot SD^{WM} \quad (5)$$

The threshold estimated was 0.69, i.e. a $\%V_A$ higher than 69% classifies data as white matter.

Parametric images of [¹⁸F]flutemetamol uptake

The grey matter VOI averages from each parametric image were compared to 2-TC DVR-1. Arterial input Logan was used to estimate the k_2' in cerebel-

lar cortex, with a cohort mean of $0.049 \pm 0.010 \text{ min}^{-1}$ (range 0.036 - 0.074 min^{-1}). The inclusion of k_2' in the generation of reference Logan parametric images had no major effect on slope and intercept, although the highest R^2 was achieved when including each subject's individual k_2' , compared to approximating the k_2' with the cohort mean or without correction for k_2' . Clearance rates determined with 2-TC ranged between 0.033 and 0.13 min^{-1} , thus covered well by the definition of basis functions in the RPM methods.

Pre-filtering of the dynamic data improved the correlation with 2-TC for all multilinear reference models, as well as for the reference Logan where k_2' was based on the cohort mean. Correlation of basis function methods RPM and RPM2 with 2-TC decreased slightly after pre-filtering was applied.

High correlations were found between 2-TC and the parametric methods for pre-filtered MRTM2, reference Logan with individual k_2' (with and without pre-filter), pre-filtered reference Logan with cohort mean k_2' , followed by RPM and SUVR without pre-filter, with R^2 ranging from 0.95 to 0.98. Slopes of the regression line for these models ranged from 0.89-1.08, with the exception of SUVR, which had a slope of 1.22. This supports the use of SUVR as a simplified means for quantification of [^{18}F]flutemetamol, validated previously by Nelissen et al. [97], also in a voxel-wise approach. The parametric images of the different models from a subject with pAD are shown in Figure 10, selecting either the unfiltered or pre-filtered version of each model that had the highest correlation to 2-TC quantification.

V_T extracted from the 16 grey matter regions and cerebellar cortex applied to the SA parametric images using 5 basis functions correlated well with V_T from VOI-based SA using 50 basis functions without correction for PVE (Pearson's $r = 0.97$, slope = 0.99). There was a significant correlation between the voxel-based estimation of DVR-1 using cerebellar cortex as reference region and V_A across subjects and regions (Pearson's $r = 0.68$, $p < 0.0001$). The voxel-based DVR-1 also correlated well across all subjects with voxel-based BP_{ND} using RPM (Pearson's $r = 0.93$, slope = 0.85).

For adaptation of the VOI-based threshold to voxel-based analysis, iterations were made starting with the VOI-based threshold, with the aim of finding a threshold that did not over-classify grey matter voxels as white matter and vice versa, as compared to MRI segmentation. $\%V_A = 60\%$ was chosen as a threshold for generation of parametric images. Five parametric images were created:

- $V_T - \text{SA}$ estimated V_T in all voxels
- $V_A - V_T$ of component A in all voxels
- $V_T^{\text{GM}} - \text{SA}$ estimated V_T in voxels with $\%V_A < 60\%$ (grey matter voxels)
- $V_T^{\text{WM}} - \text{SA}$ estimated V_T in voxels with $\%V_A \geq 60\%$ (all voxels)
- $V_A^{\text{GM}} - V_T$ of component A in voxels with $\%V_A < 60\%$ (grey matter voxels)

Examples of V_T , V_A , V_T^{GM} , V_T^{WM} and V_A^{GM} are shown in Figure 11 for representative [^{18}F]flutemetamol negative and positive subjects.

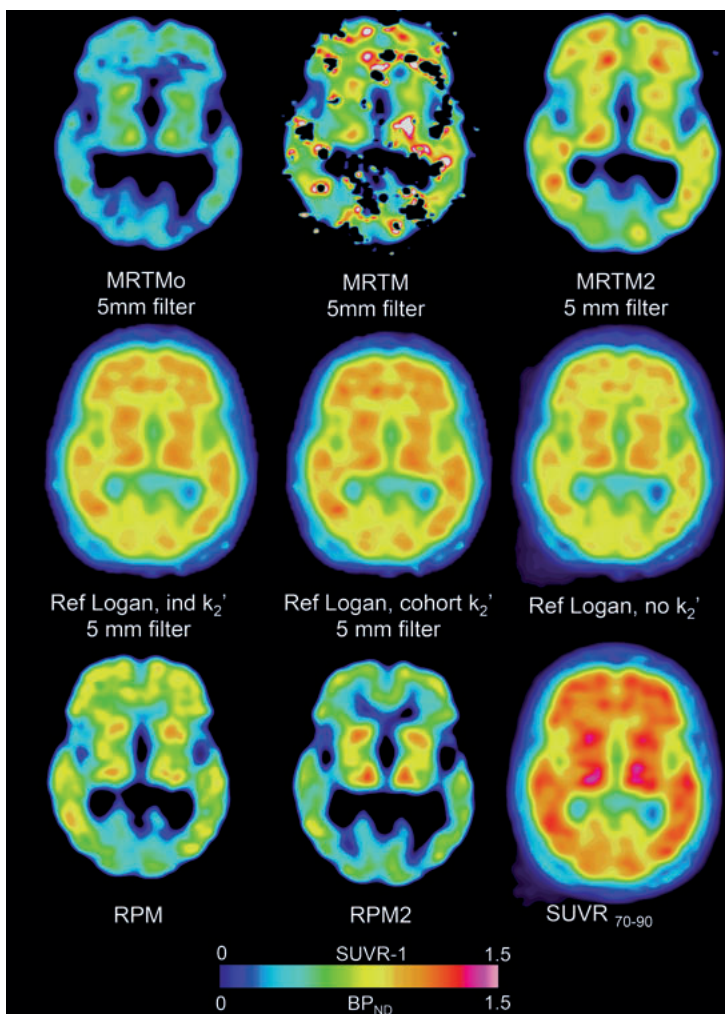


Figure 10. Examples of parametric images from a pAD subject using methods studied in Paper I. Images are either pre-filtered or without applied pre-filter based on which of the two correlated best with 2-TC quantification as indicated in the figure. Top row: multilinear reference tissue model images (from left to right): MRTMo, MRTM and MRTM2. Middle row: reference Logan images (from left to right): with correction for k_2' using individually estimated values, using cohort mean of k_2' and without correction for k_2' . Bottom row (from left to right): RPM, RPM2 and SUVR over 70-90 min.

Simulation studies

The estimated parameters from the 2-TC modelling were used as input for the simulation studies. When noise was added corresponding to the noise in VOI TACs, strong correlations were seen between the true values and the model estimates for RPM, SUVR and reference Logan as well as the 2-TC

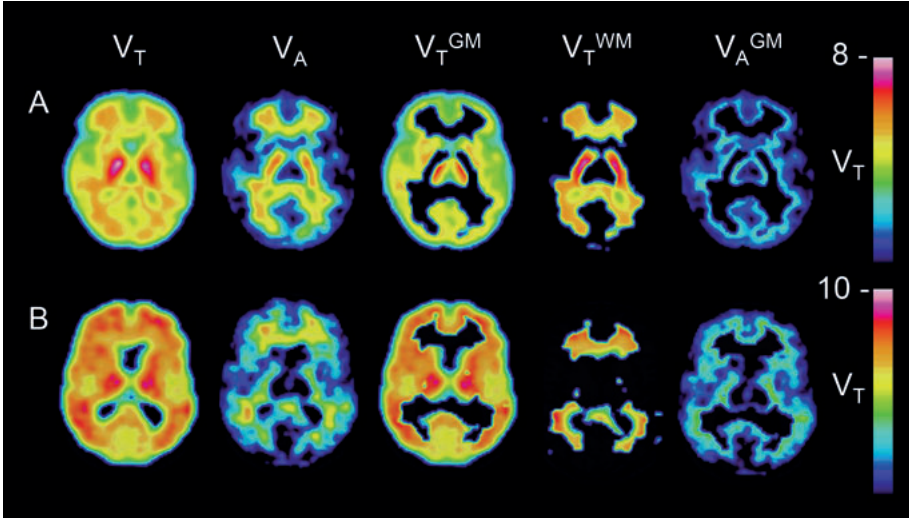


Figure 11. Examples of SA parametric images showing (from left to right): V_T , V_T from only the slow component A (V_A), V_T in voxels classified as grey matter, V_T in voxels classified as white matter and V_T from only the slow component A in voxels classified as grey matter in A) a [^{18}F]flutemetamol negative subject without apparent β -amyloid accumulation and B) in a [^{18}F]flutemetamol positive subject.

BP_{ND} and DVR-1 (RPM $R^2 = 0.99$, SUVR $R^2 = 0.97$, reference Logan $R^2 = 0.96$, 2-TC BP_{ND} $R^2 = 0.94$ and 2-TC DVR-1 $R^2 = 0.91$). SRTM, however, performed poorly ($R^2 = 0.18$), failing to find an appropriate fit of the model to the data in approximately 50% of the simulations. The highest accuracy was found for the target-to-reference-ratio (SUVR-1) and reference Logan, compared to SUVR-1 and DVR-1, respectively.

With a higher noise level added, reflecting the noise of a voxel TAC, the correlation was lower across all models demonstrating the main challenge with parametric imaging. RPM showed the highest correlation, followed by SUVR and reference Logan.

The simulations of PVE in Paper II using Gaussian smoothing had similar effects on the positive and negative phantom image, resulting in a recovery of 64% and 68% in grey matter, 68% and 71% in white matter and 79% and 77% in cerebellar cortex in the positive and negative phantom, respectively.

PVE resulted in a 21% decrease of V_T , estimated using SA in grey matter in the positive phantom, but only 6% decrease in the grey matter of the negative phantom. V_T of white matter decreased with 7% in the positive phantom and 12% in the negative phantom due to simulated PVE. V_T in cerebellar cortex decreased with 5% in the positive phantom and 9% in the negative phantom. The $\%V_A$ increased from 38 to 44% in grey matter of the positive phantom, and from 0 to 32% in the negative phantom. In white matter the $\%V_A$ decreased from 82 to 71% in the positive phantom, and from 92 to 81% in the negative phantom.

Validation of [^{18}F]flutemetamol with neuropathology

In vivo cortical biopsies

[^{18}F]Flutemetamol quantitative assessment vs. histopathology

The contralateral, ipsilateral and composite SUVR was significantly associated with the biopsy sample β -amyloid level, determined as the percentage of brain tissue section staining positive for β -amyloid with 4G8 (Pearson's $r = 0.86$, $r = 0.82$ and $r = 0.85$, respectively) in the 15 patients with iNPH included in Paper IV. Time between biopsy and PET imaging did not significantly affect β -amyloid levels.

In Paper V, all data from four pooled studies were included. The SUVR type with the largest area under the ROC curve (ROC AUC) was the composite SUVR_{CER} for three of the four SOTs (overall pathology ROC AUC = 1.00, BSS ROC AUC = 0.98, and Thioflavin S ROC AUC = 0.95). For the fourth pathology SOT, the 4G8 percentage area, the ipsilateral SUVR_{CER} had the largest ROC AUC (0.85). All ROC curves are shown in Figure 12.

The composite SUVR_{CER} vs. overall pathology also had the largest Youden index (1.00). For the other three pathology SOTs, the SUVR types with the largest Youden index were the contralateral SUVR_{PONS} vs. BSS (0.93), the composite SUVR_{CER} vs. Thioflavin S (0.84), and contralateral SUVR_{CER} vs. 4G8 (0.68).

The maximum Youden indices were used to define the optimal SUVR cut-off for estimation of sensitivity and specificity of each SUVR/SOT pair. The numbers of FN and FP results were lowest using the overall pathology SOT, and 100% PPV were only found using the overall pathology SOT (in ipsilateral and composite SUVR_{CER}, and composite SUVR_{PONS}). The proportions of FP were substantially greater than the proportions of FN for each of the 3 stains individually.

The SUVR type with the highest sum of sensitivity and specificity for each SOT was composite SUVR_{CER} vs. overall pathology (2.00), contralateral SUVR_{PONS} vs. BSS (1.93), composite SUVR_{CER} vs. Thioflavin S (1.84), and contralateral SUVR_{CER} vs. 4G8 (1.68). Using 4G8 as SOT, [^{18}F]flutemetamol had a high sensitivity with all SUVR types (> 88.9%), similar to that for the other pathology SOTs, but specificity was low (50.0 - 86.5%) as were accuracy and PPV. All SUVR types had a 100% NPV compared to BSS SOT, with composite SUVR_{CER} showing 100% accuracy for all SOTs, except 4G8.

[^{18}F]Flutemetamol visual assessment vs. histopathology

Four of the 15 patients in Paper IV had abnormal levels of β -amyloid according to the overall pathology assessment and visual assessment of [^{18}F]flutemetamol images. Using the overall pathology assessment as SOT, the visual assessment demonstrated 100% sensitivity and 100% specificity.

The tissue sections of one of the subjects could not be evaluated using BSS. In the remaining 14 subjects, the sensitivity was 100% and the specificity was 91% by visual assessment when BSS sections were used as SOT. With Thioflavin S used as SOT, the visual assessment had 67% sensitivity, and a specificity of 100%.

In the pooled analysis in Paper V, comparison of the performance of visual and quantitative assessment of [^{18}F]flutemetamol was shown to be dependent on the choice of SOT. The sum of sensitivity and specificity was greater for visual assessment than for all of the six SUVR types when using BSS as the SOT. However, with 4G8 or Thioflavin S used as SOT, the sum of sensitivity and specificity was greater for SUVR than visual assessment for all or the majority of the SUVR types (6/6 for 4G8, 5/6 for Thioflavin S). The visual assessment had significantly better specificity than four SUVR types compared to 4G8 SOT, and one compared to Thioflavin S. However, higher sensitivity using SUVR resulted in a higher sum of sensitivity and specificity for the quantitative assessments. Using overall pathology as the SOT, performance of visual and quantitative assessments were similar, with the sum of sensitivity and specificity of the visual assessment higher than two, lower than two, and equal to two of the six SUVR types.

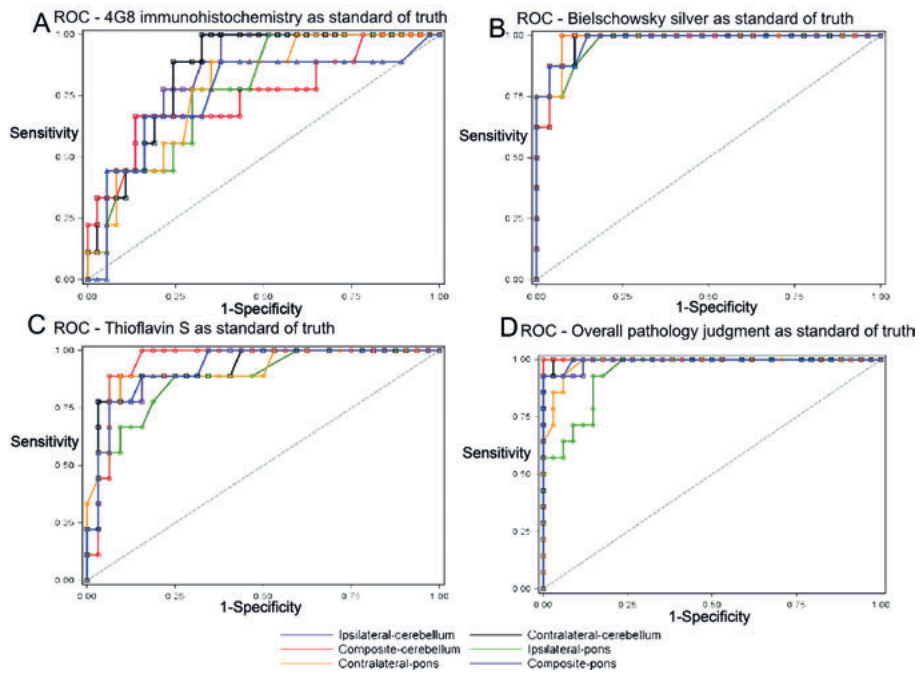


Figure 12. Receiver operating characteristics curves for each of the four pathology SOTs and six SUVR types, A) 4G8 IHC, B) BSS, C) Thioflavin S and D) overall pathology assessment. Purple: ipsilateral, black: contralateral and red: composite SUVR_{CER}. Green: ipsilateral, orange: contralateral and blue: composite SUVR_{PONS}.

Post mortem tissue sampling

[¹⁸F]Flutemetamol visual assessments

Positive [¹⁸F]flutemetamol visual assessments were associated with high Braak-NFT stages, high CERAD neuritic plaques scores and intermediate to high degrees of AD pathology according to the NIA-AA criteria. Subjects with a negative [¹⁸F]flutemetamol visual assessment showed no or low degrees of NFT and neuritic plaque pathology as well as no or low degrees of AD pathology according to the NIA-AA criteria. All β-amyloid phase 5 cases and most phase 4 were rated as positive in the visual assessment of [¹⁸F]flutemetamol images, whereas all subjects with β-amyloid phase 0, 1, and 2 were rated as negative. A third of the subjects with β-amyloid phase 3 were rated as positive. The total number of subjects, as well as the number of positive and negative reads, within β-amyloid phases and according to clinicopathologic status are summarized in Table 4.

Positive [¹⁸F]flutemetamol visual assessments were obtained in all cases with AD-type mixed dementia, i.e. cases with intermediate to high AD pathology according to the NIA-AA criteria and significant signs of a second dementing disorder, and in 96.2% of the pure AD cases. One subject classified as AD according to the NIA-AA criteria was rated as [¹⁸F]flutemetamol negative in the visual assessment, however this case was shown only to exhibit β-amyloid phase 3.

One of four p-pre-AD cases exhibited a positive [¹⁸F]flutemetamol PET scan, and this was the only p-pre-AD with a β-amyloid phase above 3. Five of 23 subjects classified as non-AD dementia according to the NIA-AA criteria were rated as positive in the visual assessment, all with β-amyloid phase 3 or 4.

β-amyloid phases had a significant influence on the [¹⁸F]flutemetamol uptake pattern as determined in the visual assessment, according to the logistic regression model controlling for age, sex, and scan-death interval, whereas NFT stages did not show a significant effect on the uptake (β-amyloid phases: $p = 0.006$; Braak-NFT stages: $p = 0.092$).

Table 4. Summary of the subject classification according to clinicopathologic status, β-amyloid phase and visual [¹⁸F]flutemetamol PET assessment

| Clinicopathologic classification | β-amyloid phase | | | | | | |
|----------------------------------|---|-----------|-----------|---------|---------|---------|---------|
| | Total N (N positive PET / N negative PET) | | | | | | |
| | N | 5 | 4 | 3 | 2 | 1 | 0 |
| Symptomatic AD | 26 (25/1) | 16 (16/0) | 9 (9/0) | 1 (0/1) | 0 | 0 | 0 |
| AD-type mixed dementia | 12 (12/0) | 7 (7/0) | 4 (4/0) | 1 (1/0) | 0 | 0 | 0 |
| Non-AD dementia | 23 (5/18) | 0 | 5 (3/2) | 5 (2/3) | 5 (0/5) | 4 (0/4) | 4 (0/4) |
| p-pre-AD | 4 (1/3) | 0 | 1 (1/0) | 2 (0/2) | 0 | 1 (0/1) | 0 |
| Non-AD controls | 3 (0/3) | 0 | 0 | 0 | 0 | 0 | 3 (0/3) |
| Total | 68 (43/25) | 23 (23/0) | 19 (17/2) | 9 (3/6) | 5 (0/5) | 5 (0/5) | 7 (0/7) |

[¹⁸F]Flutemetamol uptake patterns identified symptomatic AD cases including those with AD-type mixed pathology rather than p-pre-AD and non-AD controls ($p = 0.008$). Likewise, AD and AD-type mixed dementia combined were distinguished from pure non-AD dementias ($p = 0.002$). Subjects with p-pre-AD were not statistically different from the non-AD control subjects in [¹⁸F]flutemetamol visual assessment outcome ($p = 1.0$, Fisher’s exact test).

[¹⁸F]Flutemetamol quantitative assessments

In the 32 subjects where β -amyloid percentage area was determined using 4G8, there was a significant correlation between $SUVR_{CER}$ and β -amyloid deposition (Pearson’s $r = 0.66$).

Overall, cases with β -amyloid phases 4 and 5 had significantly higher composite SUVR than those in lower phases ($p \leq 0.006$) and differences in the $SUVR_{CER}$ levels confirmed the distinction of AD cases from non-AD control subjects and non-AD dementia cases ($p \leq 0.001$). Composite $SUVR_{CER}$ did not show differences among individual β -amyloid phase 0–2 subjects and subjects with p-pre-AD were not distinguished from non-AD control subjects based on $SUVR_{CER}$ ($p = 0.655$). The average SUVR and standard deviations within groups based on clinicopathologic classification and β -amyloid phases are shown in Figure 13.

An $SUVR_{CER}$ cut-off of 1.6 was defined, based on the agreement with the visual assessments. Based on this cut-off, three of the 43 subjects rated as positive were below and three of the 25 subjects rated as negative were above, 88.1% of phase 4-5 subjects had $SUVR_{CER} > 1.6$, while 44.4% of phase 3 subjects and only 11.8% of phase 0-2 subjects had $SUVR_{CER} > 1.6$.

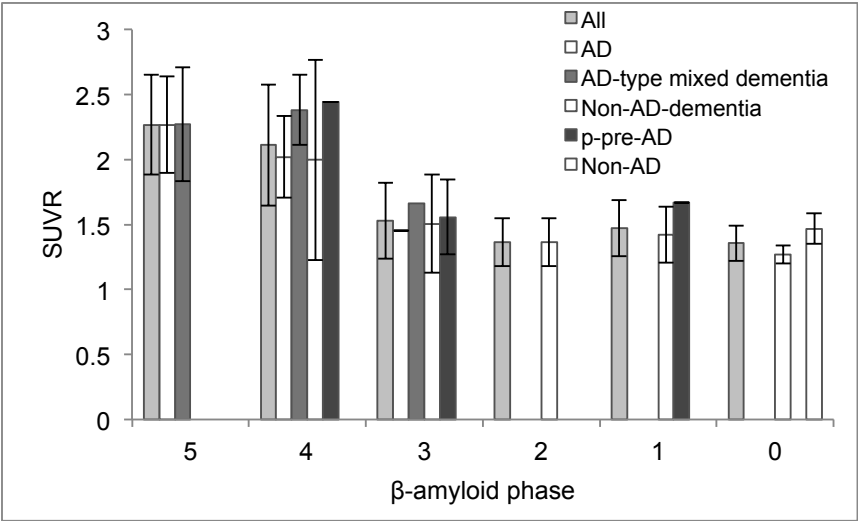


Figure 13. Average composite $SUVR_{CER}$, with standard deviations, based on β -amyloid phase and clinicopathologic classification. Data points without error-bars represent the value of a single subject.

Discussion

The work included in this thesis highlights that the use of [^{18}F]flutemetamol goes beyond that of the visual assessment specified for the clinical setting. Several quantitative approaches have been validated, both on a regional and voxel-based level, confirming the applicability of different methods with a range of complexity from static SUVR to SA. Among the parametric models investigated in Paper I, the model correlating best with compartment modelling was the voxel-wise reference Logan graphical analysis, after applied pre-filtering and using an individually determined correction for reference region k_2' . In spite of this, the benefits of this particular parametric method are limited compared to others showing slightly lower correlation with 2-TC, as it requires arterial blood sampling for estimation of k_2' which complicates the scanning procedure and reduces patient comfort considerably. MRTM suffered especially from extreme value artefacts, but these decreased when the data was filtered before application of the model, through the addition of a Gaussian filter to the dynamic data resulting in a spatial resolution of approximately 7 mm FWHM. This increased the correlation with 2-TC estimates for the majority of the graphical models, where sensitivity to noise has been previously indicated [13]. It should be noted however, that with the addition of such a pre-filter, the spatial resolution of the image data is decreased. In image data with the original spatial resolution of 5 mm, the addition of a 5 mm filter results in a lower spatial resolution of approximately 7 mm, which subsequently increases the PVE.

It has been shown here, both through comparisons with 2-TC estimates and using simulations, that SRTM is not appropriate for quantification of [^{18}F]flutemetamol uptake in spite of apparent good fitting of the model to the experimental data. This may be due to the fact that one of the assumptions of SRTM is that the kinetics both in target and reference region should be best described by a 1-TC [14], which is not the case for [^{18}F]flutemetamol. It has previously been demonstrated that the bias introduced by deviations from this assumption is dependent on the magnitude of the true BP_{ND} [124].

While SUVR has been demonstrated in this thesis to correlate well with 2-TC estimates, it is important to note that in spite of high correlations for the studied time window 70-90 min, the slope is notably higher than 1. When the conditions of a true equilibrium are not fulfilled, a terminal washout rate and blood flow dependent bias is introduced in the estimated uptake compared to BP_{ND} [125]. Estimation of SUVR at the time point of the transient

equilibrium, i.e. at the peak point of specific binding which occurs earlier than the time window studied here, could result in a lower bias with $SUVR-1=BP_{ND}$, but is in turn more sensitive to capturing the correct time window during scanning and is as such less appropriate for a simplified scanning protocol in the clinical setting [126,127].

The analyses included in this thesis focusing on the kinetic properties of [^{18}F]flutemetamol, are based on a limited sample size of six individuals. To our knowledge, these are the only subjects on which [^{18}F]flutemetamol dynamic scanning has been performed together with arterial blood sampling. The fact that one of the HV subjects showed an abnormal uptake pattern, typical of AD patients, further complicates the possibility to draw conclusions as it results in only two subjects without apparent β -amyloid accumulation for comparison of the properties in different uptake profiles. As such the results, particularly from Paper II, are of an exploratory nature and larger cohorts would be needed for confirmation of findings. Paper I does not suffer as much from this limitation, as it focuses on the range of uptake from low to high, rather than group comparisons.

In Paper II, one of the objectives was to investigate the kinetic properties of [^{18}F]flutemetamol uptake in white matter. In spite of the absence of β -amyloid accumulation in the white matter, it often exhibits a high uptake of fluorine-18 labelled β -amyloid ligands. This has been hypothesized to be due to the higher lipophilicity of fluorine-18 labelled compounds compared to carbon-11 labelled compounds [128], but may also be due to binding to myelin proteins in β -sheet conformations [108,110]. SA of [^{18}F]flutemetamol in Paper II indicated that the uptake in white matter is represented by the same kinetic component as binding to β -amyloid. While this does not prove that the white matter uptake is related to specific binding to myelin proteins, the finding suggests the need to further characterize this binding process *in vitro*, as well as in larger study groups in order to investigate the ability to detect demyelination processes using [^{18}F]flutemetamol.

The component detection of SA has been indicated to be sensitive to noise in the data. For low clearance rate basis functions, this would result in the shifting of components as well as detection of false components in the system. Bias-correction utilizing bootstrapping has been shown to lower the bias, but at the cost of increased variance [24]. Another approach is to apply numerical filtering [22] where coefficients below a certain cut-off frequency $\beta_{cut-off}$ are summed, to compensate for noise in the data. Our analyses focused on total grey matter, total white matter and the cerebellar cortex. The size of the VOIs used to study the total grey and white matter results in data with low noise, especially for the high uptake in the grey matter of subjects with apparent β -amyloid accumulation and the white matter of all subjects. In the VOIs with lower count rates and consequently higher noise, i.e. the cerebellar cortex and grey matter of subjects without apparent β -amyloid accumulation, the slow component was not detected at all. Nor were any peaks detect-

ed near the limit that could indicate a shift of the components. The basis function with the lowest rate was defined as $\beta \leq 0.0111 \text{ min}^{-1}$ which is equal to $1/T$ where T is the end time of the scanning interval [23]. This corresponds in effect to the numerical filtering proposed by Cunningham et al. [22]. This definition of the lowest rate basis function does not allow for any separation of reversible and irreversible kinetics, but instead combines all kinetics with slower rates than $\beta = 0.0111 \text{ min}^{-1}$. However, analyses using compartment modelling here and previously published [97] have shown that the kinetics are best described by reversible models, thus indicating that while very slow, the nature of the binding is reversible during the studied time window.

The complexity of β -amyloid pathology in AD, with respect to the various plaque types and varying distribution and density, further complicates the establishment of a simple relationship between β -amyloid neuropathology assessments and [^{18}F]flutemetamol binding. The β -amyloid phase, describing distribution, were shown to have a significant association with the uptake pattern of [^{18}F]flutemetamol in Paper VI. The association with the CERAD classification, describing the density, was however not investigated due to collinearity with β -amyloid phases.

While the progression of β -amyloid accumulation in phases as described by Thal et al. [52] also describes an increasing regional density, the analyses of Paper VI were limited to the global uptake of [^{18}F]flutemetamol as assessed visually or by means of the composite SUVR. As such, no analysis of the correlation between increasing regional density of β -amyloid in the different phases of β -amyloid accumulation with regional SUVR was included in Paper VI.

The impact of the variety of different β -amyloid plaque types is also demonstrated by the range in sensitivity and specificity estimates, which are dependent on the choice of neuropathological SOT due to different affinity of these to the various β -amyloid plaque types. This contradicts the concept of an SOT as an absolute truth to test the hypothesis against. In standard practice, a combination of staining techniques is typically used over a single method as they differ in their ability to detect different types of β -amyloid formations. As a result, there is no clear-cut answer to whether visual or quantitative assessments perform best in Paper V; this depends on the choice of SOT. It was shown in Paper V, however, that the best agreement between the neuropathological SOT and [^{18}F]flutemetamol classification was achieved with the most general assessments: overall pathology combining the three staining techniques and the composite SUVR providing a global estimate of the [^{18}F]flutemetamol uptake.

In Paper VI, it was concluded that only subjects with β -amyloid phase 4 and 5 can be expected to be visually assessed as [^{18}F]flutemetamol positive in the majority of cases. This makes [^{18}F]flutemetamol well suited to detect pathology in patients with AD, dementia with mixed pathology including β -

amyloid, as well as cognitively normal subjects with advanced stages of β -amyloid accumulation. In the context of identifying β -amyloid positive cognitively normal subjects for inclusion in the early stages of β -amyloid accumulation in clinical trials of anti- β -amyloid agents this however represents a limitation. In a similar study, investigating the correlation of neuropathological assessments with quantitative assessments of [^{11}C]PiB in 35 subjects, the SUVR cut-off for positivity was found to correspond approximately to β -amyloid phase 1 and 2 [77]. This contrasts the findings in our study. However, when dividing the 68 subjects into groups of phase 0-2 and phase 3-5 cases, the located optimal threshold, defined as the midpoint between these groups, was 1.57 – only slightly lower than the threshold based on the visual assessments and close to the threshold of 1.56 estimated in the Phase II study [98]. As such, quantitative assessments may provide guidance to visual assessments in borderline cases and enable the identification of earlier stages of β -amyloid accumulation.

While cerebellar cortex and pons only exhibit β -amyloid accumulation in phase 5 [52,119], this may result in underestimation of the [^{18}F]flutemetamol binding using reference regions in late stages of AD. This could contribute to the lack of difference in SUVR between subjects classified as phase 4 and 5 in Paper VI. It has been shown however, that the cerebellar β -amyloid load is characterized mainly by diffuse plaques in the molecular layer and denser plaques in the Purkinje and granular cell layers, with diffuse plaques only weakly detected by 6-CN-PiB histofluorescence, [74,129]. Whether this applies also to [^{18}F]flutemetamol has not been investigated to date, but two of the false positive subjects reported by Curtis et al. [99] in the [^{18}F]flutemetamol Phase III end-of-life study were subjects with the neuropathologic diagnosis of DLB with co-pathology of diffuse plaques and sparse to moderate neuritic plaques below the threshold for abnormality. This could be an indication that [^{18}F]flutemetamol has a higher affinity for the diffuse plaques than [^{11}C]PiB. Possible binding of [^{18}F]flutemetamol in the reference regions also complicates the use of SUVR as a method for evaluating changes in β -amyloid density longitudinally, such as effects of disease progression or treatment effects. The dentate nucleus remains free of β -amyloid accumulation also in phase 5, but would due to its location and size be difficult to use as a reference region in SUVR quantification. A more feasible alternative was suggested after investigating the effect of different reference regions on measuring longitudinal changes in [^{18}F]florbetapir SUVR in the ADNI study, recommending the use of subcortical cerebral white matter as reference region [130-132]. These studies, however, implied that the benefits of using white matter instead of a cerebellar reference region were due to lower sensitivity to subject positioning within the scanner, or possibly larger size, and hence better count statistics, of the reference region, rather than due the accumulation of β -amyloid in cerebellar cortex.

Future perspectives

The future use of [^{18}F]flutemetamol has two main applications: in clinical settings and in research. For clinical evaluations, the importance of β -amyloid PET imaging in general is still under debate, and Appropriate Use Criteria have been proposed by the Amyloid Imaging Taskforce. These recommend use of β -amyloid imaging when the cause of cognitive impairment in a patient is uncertain and could be explained on the basis of AD pathology and when knowledge of β -amyloid status in a patient would increase diagnostic certainty and alter clinical management [133]. While there are currently no disease-modifying treatment options, an accurate diagnosis is still crucial for the medical doctor to identify the appropriate symptom-treating medications available and to avoid inappropriate interventions and investigations. The National Health Service of the United Kingdom announced at the G8 summit in 2013 that coverage for β -amyloid for use in the ruling out of AD should be provided, and the question of Medicare coverage in the U.S. is still being debated. In Sweden, the biggest challenge to the introduction of β -amyloid imaging in the clinical setting has been the availability of tracers, but since 2014 [^{18}F]flutemetamol has been used at Karolinska University Hospital in Huddinge, Stockholm, in the clinical work-up of patients with uncertain diagnosis, similar to the recommendations by the Amyloid Imaging Taskforce. A financial interest in correctly excluding AD has also been indicated, as the cost of patient management decreases substantially in patients where the diagnosis has been correctly revised to Parkinson's disease or vascular dementia after an initial diagnosis of AD [134]. The clinical benefits of parametric imaging suggested in studies with [^{11}C]PiB have yet to be investigated for [^{18}F]flutemetamol [73]. Clinical use of [^{18}F]flutemetamol is thus far limited to the visual assessments of images, but as the experience and use of PET in the clinical setting increases, so will surely the off-label use of quantification.

Secondly, [^{18}F]flutemetamol may have a central role in research contexts. Clinical trials using anti- β -amyloid drugs have in the past been disappointing, possibly due the inclusion of subjects based on dementia status. These patients may be too far advanced with respect to the burden of β -amyloid pathology as the start of β -amyloid accumulation is thought to begin more than a decade before the cognitive decline has reached the dementia stage [135]. Recently, however, β -amyloid antibodies like aducanumab (Biogen) and solanezumab (Eli Lilly) [136-138], have shown positive results in clinical trials, slowing the cognitive decline and rate of β -amyloid accumulation. The studies focused on inclusion of subjects with prodromal and mild AD using a positive β -amyloid PET scans as part of the inclusion criteria. While visual assessments may suffice to identify β -amyloid positive subjects for inclusion in clinical trials in more advanced stages of β -amyloid accumulation, quantitative assessments are more appropriate in the longitudinal analy-

sis of disease progression and treatment effects. With the indication that positive β -amyloid PET scans are more likely in the late stages of β -amyloid accumulation, however, the need for more sensitive quantitative assessments will grow. While SA requires arterial cannulation and as such is inappropriate for clinical use, this method could be of value in the identification of early β -amyloid accumulators in clinical trial settings due to its potentially higher sensitivity owing to the possibility to filter the signal specific for β -amyloid binding in grey matter and thus potentially measure treatment effects more accurately.

Extrapolating findings from studies using other β -amyloid ligands beyond the field of AD, [^{18}F]flutemetamol may play a role in amyloidopathic disorders such as systemic amyloidosis [114,115,139] and in neurological disorders such as DLB [140]. The potential of [^{18}F]flutemetamol as a marker for white matter injuries remains to be investigated, but findings within this thesis taken into consideration together with evidence from studies using [^{11}C]PiB suggest that due to the high uptake in white matter, alterations in white matter binding may be able to serve as a proxy for white matter integrity [107,108,110,111].

The use of quantitative β -amyloid PET imaging in multi-centre research collaborations and clinical trials has become more common, and the need for standardization to account for sources of variability has been emphasized. These sources include which β -amyloid tracer is used, the scanning protocol, method of analysis, and selection of target and reference regions. A standardization approach has recently been proposed which scales results from any β -amyloid PET imaging agent to a common 100-point scale, where the unit is called Centiloid [141]. In addition to enabling the comparison of data obtained at different centres and using different tracers, this approach may allow for the subdivision of β -amyloid positivity into two ranges based on the magnitude of tracer uptake, allowing for a better stratification between the early and late phases of β -amyloid accumulation. For the application of the Centiloid scale to [^{18}F]flutemetamol data, i.e. establishing a conversion algorithm of uptake measurements to Centiloids, collection of data is needed, as defined by The Centiloid Project working group. This will enable cross-tracer comparisons and pooling of data sets providing the scientific community with larger bodies of data and potentially contributing to a greater understanding of the role of β -amyloid in the pathogenesis of AD.

Concluding remarks

The focus of this thesis has been to investigate the characteristics of [^{18}F]flutemetamol binding and quantification. The following were the main findings:

- Several parametric methods using reference regions, including SUVR, were appropriate for the quantification of [^{18}F]flutemetamol, enabling analysis without pre-definition of cortical regions of interest and without arterial blood sampling.
- SA allowed the quantification to be performed with minimal assumptions of the kinetic properties of [^{18}F]flutemetamol, both on the VOI- and voxel-level. SA of [^{18}F]flutemetamol indicated that the specific binding to β -amyloid in grey matter was characterized by a slow binding component. White matter uptake was characterized by the same slow binding component, but could be distinguished from β -amyloid binding based on the higher relative contribution to V_T .
- No significant differences were found in the behaviour of [^{18}F]flutemetamol in Japanese compared to Caucasian subjects, and as such results from studies performed in Caucasian subjects can be assumed to be equally applicable in the Japanese population.
- Visual and quantitative assessments showed good agreement with cortical biopsy histopathology. The best diagnostic effectiveness was achieved when estimating SUVR for the global uptake using a composite VOI and cerebellar cortex as reference region and using the overall pathology as SOT, combining outcomes of Thioflavin S, BSS and 4G8 IHC. A high agreement was found between [^{11}C]PiB and [^{18}F]flutemetamol.
- Autopsy pathology as classified according to the phase of β -amyloid distribution, indicated that [^{18}F]flutemetamol is able to detect phase 4 and 5 with high reliability, but that phase 3 only results in positive image assessments in approximately one-third of cases. Quantifying the uptake of [^{18}F]flutemetamol using SUVR showed a significantly higher uptake in AD cases compared to non-AD dementia and non-AD controls. Using an SUVR cut-off of 1.6, 88% of phase 4 and 5 subjects, but only 12% of phase 0-2 subjects, were above the threshold.

Summary in Swedish

Alzheimers sjukdom (AS) är den vanligast förekommande demenssjukdomen och utgör mellan 60-80% av alla diagnostiserade fall av demens och kännetecknas av gradvis försämrade kognitiva förmågor, vilket påverkar bl.a. närminne och språk. Det uppskattas att 35 miljoner människor levde med AS 2010, men i takt med ökande befolkning och livslängd, stiger antalet drabbade och man förutspår att det kommer att vara mer än 130 miljoner som lider av AS 2050. En absolut diagnos av sjukdomen kan endast ställas efter att en patient som uppvisat de typiska kognitiva symptomen avlidit, då man i hjärnvävnaden kan påvisa förekomsten av två patologier: ansamlingar av restproteinet β -amyloid utanför cellerna i β -amyloida plack och aggregat av proteinet tau inuti nervcellerna. Tidigare har läkare bara kunnat använda sig av klinisk diagnos baserad på minnestester och sjukdomshistoria för att ställa diagnos. Detta är problematiskt eftersom det kan vara svårt att skilja på symptomen från olika typer av demenssjukdomar, 70-90% av de patienter som fått den kliniska diagnosen AS har faktiskt också haft det då man tittat på patienternas hjärnvävnad efter att de avlidit. Många får även den kliniska diagnosen trots att de sedan inte uppvisar de patologier som är typiska för AS; endast 40-70% av de patienter som inte uppvisat patologin hade också fått den kliniska diagnosen utesluten.

Med den medicinska avbildningstekniken positronemissionstomografi (PET) kan man studera fysiologiska processer med hjälp av radioaktiva isotoper med kort halveringstid, t.ex. med kol-11 eller fluor-18 som har halveringstid på ungefär 20 respektive 110 min. Metodens känslighet gör att endast mycket små mängder märkta molekyler behöver administreras, och de kallas därför spårämnen eller tracers. För drygt ett decennium sedan utvecklades [^{11}C]Pittsburgh Compound B ([^{11}C]PiB) som binder till just β -amyloid och påvisar närvaron av β -amyloida plack i levande patienter med hög säkerhet. Den korta halveringstiden hos kol-11 gör att det måste finnas både en cyklotron för produktion av kol-11 och avancerade kemilaboratorier för märkningen av molekylen på samma plats som undersökningen ska göras. Den något längre halveringstiden hos fluor-18 möjliggör produktion på en plats, följt av distribution till omkringliggande sjukhus. I den här avhandlingen studerades [^{18}F]flutemetamol, en fluor-18 analog av [^{11}C]PiB, vilken nyligen godkändes av regulatoriska myndigheter i USA, EU, Japan och Korea under produktnamnet Vizamyl, som ett hjälpmedel vid utvärderingen av patienter med misstänkt AS.

Syftet med avhandlingen var att studera bindningsegenskaperna hos [^{18}F]flutemetamol. Metoder där den uppmätta radioaktivitetskoncentrationen omvandlas till en fysiologiskt relevant parameter i varje pixel med hjälp av matematiska modeller, baserade på antaganden kring tracerns egenskaper, så kallade parametriska metoder, utvärderades. Den uppmätta radioaktivitetskoncentrationen består förutom den mängd [^{18}F]flutemetamol som bundit till β -amyloid, även av radioaktivitet i blodet samt obunden fri tracer och tracer som via ospecifik bindning tillfälligt bundit till något annat i hjärnvävnaden. Därför är det önskvärt att kunna visualisera enbart den andel som bundit till β -amyloid. Flera parametriska metoder överensstämde väl med kompartment-modellering som anses vara den ”gyl-lene standarden” för PET kvantifiering. Detta gällde också en förenklad metod där radioaktivitetskoncentrationen normaliseras via ett ratio med koncentrationen i en referensregion i hjärnan där β -amyloid inte ansamlas, eller inte ansamlas förrän mycket sent i sjukdomsprocessen, t.ex cerebellum, kallat standardiserat upptagsvärdesratio (SUVR).

Med metoden spektralanalys beskrivs upptaget utifrån de detekterade kinetiska komponenterna. Till skillnad från de parametriska modellerna görs spektralanalys utan antaganden om tracerns egenskaper. Bindningen till β -amyloid i hjärnans grå substans konstaterades utgöras av en långsam komponent. Spektralanalys av [^{18}F]flutemetamols upptag i vit substans, som är högt trots avsaknad av ackumulerat β -amyloid, utgjordes även detta av samma långsamma komponent som bindningen till β -amyloid, men med ett mycket lägre inslag av snabba komponenter. I denna avhandling gjordes även en jämförelse mellan en japansk och en kaukasisk population, med slutsatsen att inga signifikanta skillnader finns mellan populationerna.

Upptaget av [^{18}F]flutemetamol jämfördes med uppmätt β -amyloid i vävnadsprover, dels i biopsier från patienter med normaltrycks-hydrocephalus, vilka har en ökad risk för AS, och dels från patienter med begränsad förväntad livslängd på grund av sjukdom. Dessa patienter undersöktes med [^{18}F]flutemetamol, och efter att de avlidit undersöktes hjärnan och klassificerades utifrån distributionen av β -amyloid, samt diagnosticerades baserat på demensstatus och patologi enligt etablerade metoder. Upptaget av [^{18}F]flutemetamol utvärderades både kvantitativt med SUVR, och visuellt som normalt eller onormalt av oberoende experter som inte hade någon kännedom om övrig patientinformation. Hög överensstämmelse observerades mellan både kvantitativ och visuell bedömning jämfört med det patologiska utlåtandet. Överlag uppvisade endast patienter i sena faser av spridningen av β -amyloid förhöjt upptag av [^{18}F]flutemetamol.

Sammanfattningsvis har de ingående arbetena i den här avhandlingen bidragit till att öka kunskapen om [^{18}F]flutemetamol, för dess användning vid utvärdering av β -amyloid.

Acknowledgements

My journey towards finalizing this thesis has been a winding one, and one that would not have been possible without the help and support of many. I would especially like to express my gratitude to my supervisors: professor Mark Lubberink, for your priceless expertise and support, and for your endless energy and good spirit, I'm forever grateful that you took me on as a student, and professor Jens Sörensen for sharing your wisdom and always having a good advice up your sleeve when needed.

My colleagues at GE Healthcare, and especially Dr Jan Wolber, without you this would never have been possible, thank you for giving me the time and freedom to pursue this. Patrick Cella for your great support and understanding. My warmest thank you also to Dr Chris Buckley, colleague, co-author and overall great person, for all our great discussions – scientific and non-scientific alike. Thank you also to all my other colleagues at the Grove Centre and in Princeton (or wherever you are now), for great input, invaluable feedback when reviewing articles; especially Dr Adrian Smith, Fred Longenecker, Dr Gill Farrar and Dr Paul Sherwin. The rest of you; you are too many to list and too good, you deserve a whole book! My GE people in Uppsala, Lennart, for all our interesting discussions, Roger, Alexandra, Örjan, Rikard, Stefan and Anders, thank you for making the long days in Boländerna interesting. Johan Lilja, my colleague but also good friend. Without you, life as a commuter would have been a drag and all those long days in Mordor were equally improved. I'm so happy we had each other!

All co-authors and collaborators outside of GE Healthcare, especially Dr Michio Senda, Dr Dietmar Thal, Dr Ville Leinonen, Dr Rik Vandenberghe and Dr Koen Van Laere. Thank you!

My amazing colleagues at the Uppsala PET Center, formerly known as Uppsala Imanet, it's been a long time since I first had the privilege of making your acquaintance, and I have always felt welcome even when our paths were temporarily separated by the corporate world. You all have a special place in my heart. A special shout-out to Maggan and Claire, our dinners are always a treat, even when they happen too seldom! Johanna Höglund, friend and confidant, I have learned so much from you.

My new and not so new colleagues @79:an, and my roommates at the hospital, especially My, Camilla, Ezgi and Karolina for welcoming me to your corner of the world.

My real life friends! Camilla, min fina vän och reskamrat. Smulan, du är en klippa bland klippor. Uppsala-tjejerna: Eva, Eva, Anna, Anna, Erika, Mia och Tove, tänk att tiden går så fort, det är snart tio år sen vi tog examen! Jag är så glad att vi fortfarande lyckas träffas så pass ofta som vi gör. Emma, en fantastisk inspiration och glädjekälla. Mina bokisar i Beat up kid book club. Karin, min hjälte, Ida och Henny, min koppling mellan då och nu. Tack alla! Ni har alla tillsammans gett mig energi och motivation för att göra det här.

Till min kära familj. Mamma & pappa, tack för att ni alltid trott på mig och stöttat mig, och tagit emot mig med öppna armar när jag behövt en andningspaus. Carin, Krister, Ellen och Olle, tack för att ni finns. Jag skulle också vilja sända ett tack till mormor, min kanske största supporter. Om du hade varit med oss idag vet jag hur stolt du skulle ha varit, säkert hade du satt in en annons i Östersunds-Posten för att berätta för alla hur glad du var för min skull. To my second family in Montreal, Ingrid, Vincent, Corinna, Robin and Leo, thank you for welcoming me into your family with open arms.

And finally, to Antoine... Without your determination my life would not have been the same. Thank you for always having my back and pushing me to be better, never taking the easy way out. And Benny, for making us a family, and being such an endless source of joy and happiness.

Bibliography

- [1] Cherry SR, Sorenson JA, Phelps ME. Physics in Nuclear Medicine. 3rd ed. Philadelphia: Saunders; 2003.
- [2] Jiang L, Tu Y, Shi H, Cheng Z. PET probes beyond (18)F-FDG. J Biomed Res 2014;28:435–46.
- [3] Jonasson M, Appel L, Engman J, Frick A, Nyholm D, Askmark H, et al. Validation of parametric methods for [11C]PE2I positron emission tomography. Neuroimage 2013;74:172–8.
- [4] Appel L, Jonasson M, Danfors T, Nyholm D, Askmark H, Lubberink M, et al. Use of 11C-PE2I PET in Differential Diagnosis of Parkinsonian Disorders. J Nucl Med 2015;56 :234–42.
- [5] Fazio P, Svenningsson P, Forsberg A, Jönsson EG, Amini N, Nakao R, et al. Quantitative Analysis of 18F-(E)-N-(3-Iodoprop-2-Enyl)-2 β -Carbofluoroethoxy-3 β -(4'-Methyl-Phenyl) Nortropane Binding to the Dopamine Transporter in Parkinson Disease. J Nucl Med 2015;56 :714–20.
- [6] Paterson LM, Tyacke RJ, Nutt DJ, Knudsen GM. Measuring endogenous 5-HT release by emission tomography: promises and pitfalls. J Cereb Blood Flow Metab 2010;30:1682–706.
- [7] Selvaraj S, Turkheimer F, Rosso L, Faulkner P, Mouchlianitis E, Roiser JP, et al. Measuring endogenous changes in serotonergic neurotransmission in humans: a [11C]CUMI-101 PET challenge study. Mol Psychiatry 2012;17:1254–60.
- [8] Mintun MA, Raichle ME, Kilbourn MR, Wooten GF, Welch MJ. A quantitative model for the in vivo assessment of drug binding sites with positron emission tomography. Ann Neurol 1984;15:217–27.
- [9] Gunn RN, Gunn SR, Cunningham VJ. Positron Emission Tomography Compartmental Models. J Cereb Blood Flow Metab 2001;21:635–52.
- [10] Logan J, Fowler JS, Volkow ND, Wolf AP, Dewey SL, Schlyer DJ, et al. Graphical Analysis of Reversible Radioligand binding from Time-Activity Measurements Applied to [N-11C-methyl]-(-)-Cocaine PET Studies in Human Subjects. J Cereb Blood Flow Metab 1990;10:740–7.
- [11] Patlak CS, Blasberg RG, Fenstermacher JD. Graphical evaluation of blood-to-brain transfer constants from multiple-time uptake data. J Cereb Blood Flow Metab 1983;3:1–7.
- [12] Patlak CS, Blasberg RG. Graphical evaluation of blood-to-brain transfer constants from multiple-time uptake data. Generalizations. J Cereb Blood Flow Metab 1985;5:584–90.
- [13] Slifstein M, Laruelle M. Effects of statistical noise on graphic analysis of PET neuroreceptor studies. J Nucl Med 2000;41:2083–8.
- [14] Lammertsma AA, Hume SP. Simplified reference tissue model for PET receptor studies. Neuroimage 1996;4:153–8.

- [15] Watabe H, Endres CJ, Breier A, Schmall B, Eckelman WC, Carson RE. Measurement of Dopamine Release with Continuous Infusion of [¹¹C]Raclopride: Optimization and Signal-to-Noise Considerations. *J Nucl Med* 2000;41:522–30.
- [16] Lammertsma AA, Bench CJ, Hume SP, Osman S, Gunn K, Brooks DJ, et al. Comparison of Methods for Analysis of Clinical [¹¹C] Raclopride Studies. *J Cereb Blood Flow Metab* 1996;16:42–52.
- [17] Cunningham VJ, Hume SP, Price GR, Ahier RG, Cremer JE, Jones A K. Compartmental analysis of diprenorphine binding to opiate receptors in the rat in vivo and its comparison with equilibrium data in vitro. *J Cereb Blood Flow Metab* 1991;11:1–9.
- [18] Wu Y, Carson RE. Noise Reduction in the Simplified Reference Tissue Model for Neuroreceptor Functional Imaging. *J Cereb Blood Flow Metab* 2002;22:1440–52.
- [19] Logan J, Fowler JS, Volkow D, Wang G, Ding Y, Alexoff DL. Distribution Volume Ratios Without Blood Sampling from Graphical Analysis of PET Data. *J Cereb Blood Flow Metab* 1996;16:834–40.
- [20] Ichise M, Liow J-S, Lu J-Q, Takano A, Model K, Toyama H, et al. Linearized reference tissue parametric imaging methods: application to [¹¹C]DASB positron emission tomography studies of the serotonin transporter in human brain. *J Cereb Blood Flow Metab* 2003;23:1096–112.
- [21] Ichise M, Ballinger JR, Golan H, Vines D, Luong A, Tsai S, et al. Noninvasive Quantification of Dopamine D2 Receptors with Iodine-123-IBF SPECT. *J Nucl Med* 1996;37:513–20.
- [22] Cunningham VJ, Jones T. Spectral Analysis of Dynamic PET Studies. *J Cereb Blood Flow Metab* 1993;13:15–23.
- [23] Turkheimer F, Moresco RM, Lucignani G, Sokoloff L, Fazio F, Schmidt K. The Use of Spectral Analysis to Determine Regional Cerebral Glucose Utilization with Positron Emission Tomography and [¹⁸F]Fluorodeoxyglucose: Theory, Implementation, and Optimization Procedures. *J Cereb Blood Flow Metab* 1994;14:406–22.
- [24] Turkheimer F, Sokoloff L, Bertoldo A, Lucignani G, Reivich M, Jaggi JL, et al. Estimation of Component and Parameter Distributions in Spectral Analysis. *J Cereb Blood Flow Metab* 1998;18:1211–22.
- [25] Thie JA. Understanding the standardized uptake value, its methods, and implications for usage. *J Nucl Med* 2004;45:1431–4.
- [26] Gunn RN, Lammertsma AA, Hume SP, Cunningham VJ. Parametric Imaging of Ligand-Receptor Binding in PET Using a Simplified Reference Region Model. *Neuroimage* 1997;6:279–87.
- [27] Soret M, Bacharach SL, Buvat I. Partial-Volume Effect in PET Tumor Imaging. *J Nucl Med* 2007;48:932–45.
- [28] Muller-Gartner HW, Links JM, Prince JL, Bryan RN, McVeigh tElliot, Leal JP, et al. Measurement of Radiotracer Concentration in Brain Gray Matter Using Positron Emission Tomography: MRI-Based Correction for Partial Volume Effects. *J Cereb Blood Flow Metab* 1992;12:571–83.
- [29] Meltzer CC, Leal JP, Mayberg HS, Wagner HN, Frost JJ. Correction of PET data for partial volume effects in human cerebral cortex by MR imaging. *J Comput Assist Tomogr* 1990;14:561–70.

- [30] Rousset OG, Ma Y, Evans a C. Correction for partial volume effects in PET: principle and validation. *J Nucl Med* 1998;39:904–11.
- [31] Su Y, Blazey TM, Snyder AZ, Raichle ME, Marcus DS, Ances BM, et al. Partial volume correction in quantitative amyloid imaging. *Neuroimage* 2015;107:55–64.
- [32] Thomas BA, Erlandsson K, Modat M, Thurfjell L, Vandenberghe R, Ourselin S, et al. The importance of appropriate partial volume correction for PET quantification in Alzheimer's disease. *Eur J Nucl Med Mol Imaging* 2011;38:1104–19.
- [33] Svarer C, Madsen K, Hasselbalch SG, Pinborg LH, Haugbøl S, Frøkjær VG, et al. MR-based automatic delineation of volumes of interest in human brain PET images using probability maps. *Neuroimage* 2005;24:969–79.
- [34] Alzheimer's Association. Alzheimer's Disease Facts and Figures. *Alzheimers Dement* 2015;11:332+.
- [35] Prince M, Wimo A, Guerchet M, Ali G-C, Wu Y-T, Prina M. World Alzheimer's Report 2015. 2015.
- [36] Alladi S, Xuereb J, Bak T, Nestor P, Knibb J, Patterson K, et al. Focal cortical presentations of Alzheimer's disease. *Brain* 2007;130:2636–45.
- [37] Petersen RC. Mild cognitive impairment as a diagnostic entity. *J Intern Med* 2004;256:183–94.
- [38] McKhann G, Drachman D, Folstein M, Katzman R, Price D, Stadlan EM. Clinical diagnosis of Alzheimer's disease: report of the NINCDS-ADRDA Work Group under the auspices of Department of Health and Human Services Task Force on Alzheimer's Disease. *Neurology* 1984;34:939–44.
- [39] Beach TG, Monsell SE, Phillips LE, Kukull W. Accuracy of the Clinical Diagnosis of Alzheimer Disease at National Institute on Aging Alzheimer Disease Centers, 2005–2010. *J Neuropathol Exp Neurol* 2012;71:266–73.
- [40] Jack CRJ, Knopman DS, Jagust WJ, Petersen RC, Weiner MW, Aisen PS, et al. Tracking pathophysiological processes in Alzheimer's disease: an updated hypothetical model of dynamic biomarkers. *Lancet Neurol* 2013;12:207–16.
- [41] Sperling RA, Aisen PS, Beckett LA, Bennett DA, Craft S, Fagan AM, et al. Toward defining the preclinical stages of Alzheimer's disease: recommendations from the National Institute on Aging-Alzheimer's Association workgroups on diagnostic guidelines for Alzheimer's disease. *Alzheimers Dement* 2011;7:280–92.
- [42] Albert MS, DeKosky ST, Dickson D, Dubois B, Feldman HH, Fox NC, et al. The diagnosis of mild cognitive impairment due to Alzheimer's disease: recommendations from the National Institute on Aging-Alzheimer's Association workgroups on diagnostic guidelines for Alzheimer's disease. *Alzheimers Dement* 2011;7:270–9.
- [43] McKhann GM, Knopman DS, Chertkow H, Hyman BT, Jack CR, Kawas CH, et al. The diagnosis of dementia due to Alzheimer's disease: recommendations from the National Institute on Aging-Alzheimer's Association workgroups on diagnostic guidelines for Alzheimer's disease. *Alzheimers Dement* 2011;7:263–9.
- [44] Dubois B, Feldman HH, Jacova C, Hampel H, Molinuevo JL, Blennow K, et al. Advancing research diagnostic criteria for Alzheimer's disease: the IWG-2 criteria. *Lancet Neurol* 2014;13:614–29.

- [45] Dubois B, Feldman HH, Jacova C, DeKosky ST, Barberger-Gateau P, Cummings J, et al. Research criteria for the diagnosis of Alzheimer's disease: revising the NINCDS-ADRDA criteria. *Lancet Neurol* 2007;6:734–46.
- [46] Dubois B, Feldman HH, Jacova C, Cummings JL, DeKosky ST, Barberger-Gateau P, et al. Revising the definition of Alzheimer's disease: A new lexicon. *Lancet Neurol* 2010;9:1118–27.
- [47] Jack CR, Knopman DS, Jagust WJ, Shaw LM, Aisen PS, Weiner MW, et al. Hypothetical model of dynamic biomarkers of the Alzheimer's pathological cascade. *Lancet Neurol* 2010;9:119–28.
- [48] Alzheimer A. Ueber eine eigenartige erkrankung der hirnrinde. *Z Gesamte Neurol Psychiatr* 1907;18:177–9.
- [49] Khachaturian ZS. Diagnosis of alzheimer's disease. *Arch Neurol* 1985;42:1097–105.
- [50] Kang J, Lemaire H-G, Unterbeck A, Salbaum JM, Masters CL, Grzeschik K-H, et al. The precursor of Alzheimer's disease amyloid A4 protein resembles a cell-surface receptor. *Nature* 1987;325:733–6.
- [51] Braak H, Braak E. Neuropathological staging of Alzheimer-related changes. *Acta Neuropathol* 1991;82:239–59.
- [52] Thal DR, Rüb U, Orantes M, Braak H. Phases of A β -deposition in the human brain and its relevance for the development of AD. *Neurology* 2002;58:1791–800.
- [53] Tierney MC, Fisher RH, Lewis AJ, Zorzitto ML, Snow WG, Reid DW, et al. The NINCDS-ADRDA Work Group criteria for the clinical diagnosis of probable Alzheimer's disease: A clinicopathologic study of 57 cases. *Neurology* 1988;38:359–64.
- [54] Mirra SS, Heyman A, McKeel D, Sumi SM, Crain BJ, Brownlee LM, et al. The Consortium to Establish a Registry for Alzheimer's Disease (CERAD): Part II. Standardization of the neuropathologic assessment of Alzheimer's disease. *Neurology* 1991;41:479–86.
- [55] The National Institute on Aging and Reagan Institute Working Group on Diagnostic Criteria for the Neuropathological Assessment of Alzheimer's Disease. Consensus Recommendations for the Postmortem Diagnosis of Alzheimer's Disease. *Neurobiol Aging* 1997;18:S1–2.
- [56] Kelényi G. Thioflavin S fluorescent and congo red anisotropic stainings in the histologic demonstration of amyloid. *Acta Neuropathol* 1967;7:336–48.
- [57] Yamaguchi H, Hirai S, Morimatsu M, Shoji M, Harigaya Y. Diffuse type of senile plaques in the brains of Alzheimer-type dementia. *Acta Neuropathol* 1988;77:113–9.
- [58] Wisniewski HM, Wen GY, Kim KS. Comparison of four staining methods on the detection of neuritic plaques. *Acta Neuropathol* 1989;78:22–7.
- [59] Jeppsson A, Zetterberg H, Blennow K, Wikkelsø C. Pathophysiology and diagnosis by CSF biomarkers. *Neurology* 2013;80:1385–92.
- [60] Devito EE, Pickard JD, Salmond CH, Iddon JL, Loveday C, Sahakian BJ. The Neuropsychology of Normal Pressure Hydrocephalus (NPH). *Br J Neurosurg* 2005;19:217–24.
- [61] Klinge P, Hellström P, Tans J, Wikkelsø C. One-year outcome in the European multicentre study on iNPH. *Acta Neurol Scand* 2012;126:145–53.

- [62] Leinonen V, Koivisto AM, Savolainen S, Rummukainen J, Tamminen JN, Tillgren T, et al. Amyloid and Tau Proteins in Cortical Brain Biopsy and Alzheimer's Disease. *Ann Neurol* 2010;68:446–53.
- [63] Hamilton R, Patel S, Lee EB, Jackson EM, Lopinto J, Arnold SE, et al. Lack of Shunt Response in Suspected Idiopathic Normal Pressure Hydrocephalus with Alzheimer Disease Pathology. *Ann Neurol* 2010;68:535–40.
- [64] Golomb J, Wiso J V, Miller DC, Boksay I, Kluger A, Weiner H, et al. Alzheimer's disease comorbidity in normal pressure hydrocephalus: prevalence and shunt response. *J Neurol Neurosurg Psychiatry* 2000;68:778–81.
- [65] Hiraoka K, Narita W, Kikuchi H, Baba T, Kanno S, Iizuka O, et al. Amyloid deposits and response to shunt surgery in idiopathic normal-pressure hydrocephalus. *J Neurol Sci* 2015;Epub ahead of print.
- [66] Klunk WE, Engler H, Nordberg A, Wang Y, Blomqvist G, Holt DP, et al. Imaging Brain Amyloid in Alzheimer's Disease with Pittsburgh Compound-B. *Ann Neurol* 2004;55:306–19.
- [67] Price JC, Klunk WE, Lopresti BJ, Lu X, Hoge J a, Ziolkko SK, et al. Kinetic modeling of amyloid binding in humans using PET imaging and Pittsburgh Compound-B. *J Cereb Blood Flow Metab* 2005;25:1528–47.
- [68] Ni R, Gillberg P-G, Bergfors A, Marutle A, Nordberg A. Amyloid tracers detect multiple binding sites in Alzheimer's disease brain tissue. *Brain* 2013;136:2217–27.
- [69] Lopresti BJ, Klunk WE, Mathis C a, Hoge J a, Ziolkko SK, Lu X, et al. Simplified quantification of Pittsburgh Compound B amyloid imaging PET studies: a comparative analysis. *J Nucl Med* 2005;46:1959–72.
- [70] McNamee RL, Yee S-H, Price JC, Klunk WE, Rosario B, Weissfeld L, et al. Consideration of optimal time window for Pittsburgh compound B PET summed uptake measurements. *J Nucl Med* 2009;50:348–55.
- [71] Yaqub M, Tolboom N, Boellaard R, Berckel BNM Van, Tilburg EW Van, Luurtsema G, et al. Simplified parametric methods for [11C] PIB studies. *Neuroimage* 2008;42:76–86
- [72] Edison P, Brooks DJ, Turkheimer FE, Archer H a., Hinz R. Strategies for the generation of parametric images of [11C]PIB with plasma input functions considering discriminations and reproducibility. *Neuroimage* 2009;48:329–38.
- [73] Zwan MD, Ossenkoppele R, Tolboom N, Beunders AJM, Kloet RW, Adri-aanse SM, et al. Comparison of Simplified Parametric Methods for Visual Interpretation of 11C-Pittsburgh Compound-B PET Images. *J Nucl Med* 2014;55:1305–7.
- [74] Ikonovic MD, Klunk WE, Abrahamson EE, Mathis C a, Price JC, Tsopelas ND, et al. Post-mortem correlates of in vivo PiB-PET amyloid imaging in a typical case of Alzheimer's disease. *Brain* 2008;131:1630–45.
- [75] Driscoll I, Troncoso JC, Rudow G, Sojkova J, Pletnikova O, Zhou Y, et al. Correspondence between in vivo 11C-PiB-PET amyloid imaging and post-mortem, region-matched assessment of plaques. *Acta Neuropathol* 2012;124:823–31.
- [76] Sojkova J, Driscoll I, Iacono D, Al E. In Vivo Fibrillar β -amyloid Detected Using [11C]PiB Positron Emission Tomography and Neuropathologic Assessment in Older Adults. *Arch Neurol* 2011;68:232–40.

- [77] Murray ME, Lowe VJ, Graff-Radford NR, Liesinger AM, Cannon A, Przybelski SA, et al. Clinicopathologic and 11C-Pittsburgh compound B implications of Thal amyloid phase across the Alzheimer's disease spectrum. *Brain* 2015;Epub ahead of print.
- [78] Leinonen V, Alafuzoff I, Aalto S, Suotunen T, Savolainen S, Nagren K, et al. Assessment of beta-Amyloid in a Frontal Cortical Brain Biopsy Specimen and by Positron Emission Tomography With Carbon 11-Labeled Pittsburgh Compound B. *Arch Neurol* 2009;65:1304–9.
- [79] Jack CR, Wiste HJ, Lesnick TG, Weigand SD, Knopman DS, Vemuri P, et al. Brain β -amyloid load approaches a plateau. *Neurology* 2013;80:890–6.
- [80] Forsberg A, Engler H, Almkvist O, Blomquist G, Hagman G, Wall A, et al. PET imaging of amyloid deposition in patients with mild cognitive impairment. *Neurobiol Aging* 2008;29:1456–65.
- [81] Food and Drug Administration. Amyvid FDA Prescribing Information 2012. http://www.accessdata.fda.gov/drugsatfda_docs/label/2012/202008s000lbl.pdf (accessed May 25, 2015).
- [82] European Medicines Agency. Amyvid EMA Summary of Product Characteristics 2014. http://www.ema.europa.eu/docs/en_GB/document_library/EPAR_-_Product_Information/human/002422/WC500137635.pdf (accessed May 25, 2015).
- [83] Food and Drug Administration. Neuraceq FDA Prescribing Information 2014. http://www.accessdata.fda.gov/drugsatfda_docs/label/2014/204677s000lbl.pdf (accessed May 25, 2015).
- [84] European Medicines Agency. Neuraceq EMA Summary of Products Characteristics 2014;http://www.ema.europa.eu/docs/en_GB/document_library/EPAR_-_Product_Information/human/002553/WC500162592.pdf (accessed May 25, 2015).
- [85] Food and Drug Administration. Vizamyl FDA Prescribing Information 2014. http://www.accessdata.fda.gov/drugsatfda_docs/label/2013/203137s000lbl.pdf (accessed May 25, 2015).
- [86] European Medicines Agency. Vizamyl EMA Summary of Product Characteristics 2014. http://www.ema.europa.eu/docs/en_GB/document_library/EPAR_-_Product_Information/human/002557/WC500172950.pdf (accessed May 25, 2015).
- [87] Schou M, Varnäs K, Sandell J, Johnström P, Cselenyi Z, Svensson S, et al. Synthesis, radiolabeling, and in vivo pharmacokinetic evaluation of the amyloid beta radioligand [11C]AZD4694 in nonhuman primates. *Mol Imaging Biol* 2014;16:173–9.
- [88] Cselenyi Z, Jönghagen ME, Forsberg A, Halldin C, Julin P, Schou M, et al. Clinical validation of 18F-AZD4694, an amyloid- β -specific PET radioligand. *J Nucl Med* 2012;53:415–24.
- [89] Mueller SG, Weiner MW, Thal LJ, Petersen RC, Jack CR, Jagust W, et al. Ways toward an early diagnosis in Alzheimer's disease: the Alzheimer's Disease Neuroimaging Initiative (ADNI). *Alzheimers Dement* 2005;1:55–66.
- [90] Weiner MW, Veitch DP, Aisen PS, Beckett LA, Cairns NJ, Cedarbaum J, et al. Impact of the Alzheimer's Disease Neuroimaging Initiative, 2004 to 2014. *Alzheimer's Dement* 2015;11:865–84.

- [91] Jansen WJ, Ossenkoppele R, Knol DL, Tijms BM, Scheltens P, Verhey FRJ, et al. Prevalence of Cerebral Amyloid Pathology in Persons Without Dementia. *JAMA* 2015;313:1924–38.
- [92] Morris JC, Roe CM, Xiong C, Fagan AM, Goate AM, Holtzman DM, et al. APOE predicts amyloid-beta but not tau Alzheimer pathology in cognitively normal aging. *Ann Neurol* 2010;67:122–31.
- [93] Mathis CA, Ikonomic MD, Debnath ML, Hamilton RL, DeKosky ST, Klunk WE. Comparison of the binding of 3'-F-PiB and PiB in human brain homogenates. *Neuroimage* 2008;41, Suppl:T113–4.
- [94] Mathis C, Lopresti B, Mason N, Price J, Flatt N, Bi W, et al. Comparison of the amyloid imaging agents [F-18]3'-F-PIB and [C-11]PIB in Alzheimer's disease and control subjects. *J Nucl Med* 2007;48:56P – 56P.
- [95] Koole M, Lewis DM, Buckley C, Nelissen N, Vandenbulcke M, Brooks DJ, et al. Whole-body biodistribution and radiation dosimetry of 18F-GE067: a radioligand for in vivo brain amyloid imaging. *J Nucl Med* 2009;50:818–22.
- [96] Senda M, Brooks D, Farrar G, Somer E, Paterson C, Sasaki M, et al. The clinical safety, biodistribution and internal radiation dosimetry of flutemetamol (18F) injection in healthy Japanese adult volunteers. *Ann Nucl Med* 2015;29:627–35.
- [97] Nelissen N, Van Laere K, Thurfjell L, Owenius R, Vandenbulcke M, Koole M, et al. Phase 1 study of the Pittsburgh compound B derivative 18F-flutemetamol in healthy volunteers and patients with probable Alzheimer disease. *J Nucl Med* 2009;50:1251–9.
- [98] Vandenberghe R, Van Laere K, Ivanoiu A, Salmon E, Bastin C, Triau E, et al. 18F-flutemetamol amyloid imaging in Alzheimer disease and mild cognitive impairment: a Phase 2 trial. *Ann Neurol* 2010;68:319–29.
- [99] Curtis C, Gamez JE, Singh U, Sadowsky CH, Villena T, Sabbagh MN, et al. Phase 3 trial of flutemetamol labeled with radioactive fluorine 18 imaging and neuritic plaque density. *JAMA Neurol* 2015;72:287–94.
- [100] Thurfjell L, Lötjönen J, Lundqvist R, Koikkalainen J, Soininen H, Walde- mar G, et al. Combination of Biomarkers: PET [18F]Flutemetamol Imaging and Structural MRI in Dementia and Mild Cognitive Impairment. *Neuro- degener Dis* 2012;10:246–9.
- [101] Wolk DA, Duara R, Sadowsky C. [18F]Flutemetamol Amyloid PET imaging: Outcome of a Phase III study in subjects with amnesic mild cognitive impairment after a 3-year follow-up. *Alzheimer's Dement* 2014;10:P898.
- [102] Hatashita S, Yamasaki H, Suzuki Y, Tanaka K, Wakebe D, Hayakawa H. [18F]Flutemetamol amyloid-beta PET imaging compared with [11C]PIB across the spectrum of Alzheimer's disease. *Eur J Nucl Med Mol Imaging* 2014;41:290–300.
- [103] Landau SM, Breault C, Joshi AD, Pontecorvo M, Mathis CA, Jagust WJ, et al. Amyloid- β Imaging with Pittsburgh Compound B and Florbetapir: Comparing Radiotracers and Quantification Methods. *J Nucl Med* 2013;54:70–7.
- [104] Villemagne VL, Mulligan RS, Pejoska S, Ong K, Jones G, O'Keefe G, et al. Comparison of 11C-PiB and 18F-florbetaben for A β imaging in ageing and Alzheimer's disease. *Eur J Nucl Med Mol Imaging* 2012;39:983–9.
- [105] Landau SM, Thomas BA, Thurfjell L, Schmidt M, Margolin R, Mintun M, et al. Amyloid PET imaging in Alzheimer's disease: a comparison of three radiotracers. *Eur J Nucl Med Mol Imaging* 2014;41:1398–407.

- [106] Rowe CC, Pejoska S, Mulligan RS, Jones G, Chan JG, Svensson S, et al. Head-to-head comparison of ¹¹C-PiB and ¹⁸F-AZD4694 (NAV4694) for β -amyloid imaging in aging and dementia. *J Nucl Med* 2013;54:880–6.
- [107] Fodero-Tavoletti MT, Rowe CC, McLean CA, Leone L, Li Q-X, Masters CL, et al. Characterization of PiB Binding to White Matter in Alzheimer Disease and Other Dementias. *J Nucl Med* 2009;50:198–204.
- [108] Stankoff B, Freeman L, Aigrot M-S, Chardain A, Dollé F, Williams A, et al. Imaging central nervous system myelin by positron emission tomography in multiple sclerosis using [methyl-¹¹C]-2-(4'-methylaminophenyl)-6-hydroxybenzothiazole. *Ann Neurol* 2011;69:673–80.
- [109] Harauz G, Ishiyama N, Hill CMD, Bates IR, Libich DS, Farès C. Myelin basic protein—diverse conformational states of an intrinsically unstructured protein and its roles in myelin assembly and multiple sclerosis. *Micron* 2004;35:503–42.
- [110] Veronese M, Bodini B, García-Lorenzo D, Battaglini M, Bongarzone S, Comtat C, et al. Quantification of [¹¹C]PIB PET for imaging myelin in the human brain: a test–retest reproducibility study in high-resolution research tomography. *J Cereb Blood Flow Metab* 2015:1–12.
- [111] De Paula Faria D, Copray S, Sijbesma JA, Willemsen AM, Buchpiguel C, Dierckx RJO, et al. PET imaging of focal demyelination and remyelination in a rat model of multiple sclerosis: comparison of [¹¹C]MeDAS, [¹¹C]CIC and [¹¹C]PIB. *Eur J Nucl Med Mol Imaging* 2014;41:995–1003.
- [112] Glodzik L, Rusinek H, Li J, Zhou C, Tsui W, Mosconi L, et al. Reduced retention of Pittsburgh compound B in white matter lesions. *Eur J Nucl Med Mol Imaging* 2015;42:97–102.
- [113] Johnson KA, Gregas M, Becker JA, Kinnecom C, Salat DH, Moran EK, et al. Imaging of amyloid burden and distribution in cerebral amyloid angiopathy. *Ann Neurol* 2007;62:229–34.
- [114] Antoni G, Lubberink M, Estrada S, Axelsson J, Carlson K, Lindsjö L, et al. In vivo visualization of amyloid deposits in the heart with ¹¹C-PIB and PET. *J Nucl Med* 2013;54:213–20.
- [115] Lhommel R, Sempoux C, Ivanoiu A, Michaux L. Is ¹⁸F-Flutemetamol PET/CT Able to Reveal Cardiac Amyloidosis? *Clin Nucl Med* 2014;39:747–9.
- [116] Edison P, Rowe CC, Rinne JO, Ng S, Ahmed I, Kemppainen N, et al. Amyloid load in Parkinson's disease dementia and Lewy body dementia measured with [¹¹C]PIB positron emission tomography. *J Neurol Neurosurg Psychiatry* 2008;79:1331–8.
- [117] Landt J, D'Abbrera JC, Holland AJ, Aigbirhio FI, Fryer TD, Canales R, et al. Using positron emission tomography and Carbon 11-labeled Pittsburgh Compound B to image Brain Fibrillar β -amyloid in adults with down syndrome: safety, acceptability, and feasibility. *Arch Neurol* 2011;68:890–6.
- [118] Hong YT, Veenith T, Dewar D, Outtrim JG, Mani V, Williams C, et al. Amyloid imaging with carbon 11-labeled pittsburgh compound B for traumatic brain injury. *JAMA Neurol* 2014;71:23–31.
- [119] Alafuzoff I, Thal D, Arzberger T, Bogdanovic N, Al-Sarraj S, Bodi I, et al. Assessment of β -amyloid deposits in human brain: a study of the BrainNet Europe Consortium. *Acta Neuropathol* 2009;117:309–20.

- [120] Hyman BT, Phelps CH, Beach TG, Bigio EH, Cairns NJ, Carrillo MC, et al. National Institute on Aging–Alzheimer’s Association guidelines for the neuropathologic assessment of Alzheimer’s disease. *Alzheimer’s Dement* 2012;8:1–13.
- [121] Andersson JLR. A Rapid and Accurate Method to Realign PET Scans Utilizing Image Edge Information. *J Nucl Med* 1995;36:657–69.
- [122] Andersson JLR, Thurfjell L. Implementation and Validation of a Fully Automatic System for Intra- and Interindividual Registration of PET Brain Scans. *J Comput Assist Tomogr* 1997;21:136–44.
- [123] Klumpers UMH, Boellaard R, Veltman DJ, Kloet RW, Hoogendijk WJG, Lammertsma AA. Parametric [¹¹C]flumazenil images. *Nucl Med Commun* 2012;33:422–30.
- [124] Salinas CA, Searle GE, Gunn RN. The simplified reference tissue model: model assumption violations and their impact on binding potential. *J Cereb Blood Flow Metab* 2014.
- [125] Carson RE, Channing M a, Blasberg RG, Dunn BB, Cohen RM, Rice KC, et al. Comparison of bolus and infusion methods for receptor quantitation: application to [¹⁸F]cyclofoxy and positron emission tomography. *J Cereb Blood Flow Metab* 1993;13:24–42.
- [126] Ito H, Hietala J, Blomqvist G, Halldin C, Farde L. Comparison of the Transient Equilibrium and Continuous Infusion Method for Quantitative PET Analysis of [¹¹C]Raclopride Binding. *J Cereb Blood Flow Metab* 1998;18:941–50.
- [127] Farde L, Eriksson L, Blomquist G, Halldin C. Kinetic Analysis of Central [¹¹C]Raclopride Binding to D2-Dopamine Receptors Studied by PET - A Comparison to the Equilibrium Analysis. *J Cereb Blood Flow Metab* 1989;9:696–708.
- [128] Sebai S, Baciú M, Ces O, Clarke J, Cunningham V, Gunn R, et al. To lipophilicity and beyond—towards a deeper understanding of radioligand non-specific binding. *Neuroimage* 2006;31:T56.
- [129] Joachim CL, Morris JH, Selkoe DJ. Diffuse senile plaques occur commonly in the cerebellum in Alzheimer’s disease. *Am J Pathol* 1989;135:309–19.
- [130] Landau SM, Fero A, Baker SL, Koeppe R, Mintun M, Chen K, et al. Measurement of Longitudinal β -Amyloid Change with ¹⁸F-Florbetapir PET and Standardized Uptake Value Ratios. *J Nucl Med* 2015;56:567–74.
- [131] Chen K, Roontiva A, Thiyyagura P, Lee W, Liu X, Ayutyanont N, et al. Improved Power for Characterizing Longitudinal Amyloid- β PET Changes and Evaluating Amyloid-Modifying Treatments with a Cerebral White Matter Reference Region. *J Nucl Med* 2015;56:560–6.
- [132] Brendel M, Högenauer M, Delker A, Sauerbeck J, Bartenstein P, Seibyl J, et al. Improved longitudinal [¹⁸F]-AV45 amyloid PET by white matter reference and VOI-based partial volume effect correction. *Neuroimage* 2015;108:450–9.
- [133] Johnson KA, Minoshima S, Bohnen NI, Donohoe KJ, Foster NL, Herscovitch P, et al. Appropriate use criteria for amyloid PET: A report of the Amyloid Imaging Task Force, the Society of Nuclear Medicine and Molecular Imaging, and the Alzheimer’s Association. *Alzheimer’s Dement* 2013;9:E1–16.

- [134] Hunter CA, Kirson NY, Desai U, Cummings AKG, Faries DE, Birnbaum HG. Medical costs of Alzheimer's disease misdiagnosis among US Medicare beneficiaries. *Alzheimer's Dement* 2015;11:887–95.
- [135] Rowe CC, Ellis KA, Rimajova M, Bourgeat P, Pike KE, Jones G, et al. Amyloid imaging results from the Australian Imaging, Biomarkers and Lifestyle (AIBL) study of aging. *Neurobiol Aging* 2010;31:1275–83.
- [136] alzforum.com. Biogen Antibody Buoyed by Phase 1 Data and Hungry Investors 2015. <http://www.alzforum.org/news/conference-coverage/biogen-antibody-buoyed-phase-1-data-and-hungry-investors> (accessed August 29, 2015).
- [137] Reardon S. Antibody drugs for Alzheimer's show glimmers of promise. *Nat* 2015;523:509–10.
- [138] Siemers ER, Sundell KL, Carlson C, Case M, Sethuraman G, Liu-Seifert H, et al. Phase 3 solanezumab trials: Secondary outcomes in mild Alzheimer's disease patients. *Alzheimer's Dement* 2015;Epub ahead of print.
- [139] Kero T, Lindsjö L, Sörensen J, Lubberink M. Accurate analysis and visualization of cardiac 11C-PIB uptake in amyloidosis with semiautomatic software. *J Nucl Cardiol* 2015;Epub ahead of print.
- [140] Villemagne VL, Ong K, Mulligan RS, Holl G, Pejoska S, Jones G, et al. Amyloid Imaging with 18F-Florbetaben in Alzheimer Disease and Other Dementias. *J Nucl Med* 2011;52 :1210–7.
- [141] Klunk WE, Koeppe RA, Price JC, Benzinger TL, Devous Sr. MD, Jagust WJ, et al. The Centiloid Project: Standardizing quantitative amyloid plaque estimation by PET. *Alzheimer's Dement* 2015;11:1–15.e4.

Acta Universitatis Upsaliensis

*Digital Comprehensive Summaries of Uppsala Dissertations
from the Faculty of Medicine 1139*

Editor: The Dean of the Faculty of Medicine

A doctoral dissertation from the Faculty of Medicine, Uppsala University, is usually a summary of a number of papers. A few copies of the complete dissertation are kept at major Swedish research libraries, while the summary alone is distributed internationally through the series Digital Comprehensive Summaries of Uppsala Dissertations from the Faculty of Medicine. (Prior to January, 2005, the series was published under the title "Comprehensive Summaries of Uppsala Dissertations from the Faculty of Medicine".)



ACTA
UNIVERSITATIS
UPSALIENSIS
UPPSALA
2015

Distribution: publications.uu.se
urn:nbn:se:uu:diva-262019